

Gene-SGAN: a method for discovering disease subtypes with imaging and genetic signatures via multi-view weakly-supervised deep clustering

Zhijian Yang^{1,2}, Junhao Wen^{1,3}, Ahmed Abdulkadir⁴, Yuhan Cui¹, Guray Erus¹, Elizabeth Mamourian¹, Randa Melhem¹, Dhivya Srinivasan¹, Sindhuja T. Govindarajan¹, Jiong Chen¹, Mohamad Habes⁵, Colin L. Masters⁶, Paul Maruff⁶, Jurgen Fripp⁷, Luigi Ferrucci⁸, Marilyn S. Albert^{9†}, Sterling C. Johnson¹⁰, John C. Morris¹¹, Pamela LaMontagne¹², Daniel S. Marcus¹², Tammie L.S. Benzinger^{11,12}, David A. Wolk¹³, Li Shen¹⁴, Jingxuan Bao¹⁴, Susan M. Resnick^{15†}, Haochang Shou¹⁴, Ilya M. Nasrallah^{1,16}, Christos Davatzikos^{1†*}, for the Alzheimer's Disease Neuroimaging Initiative, the Preclinical AD Consortium, the Baltimore Longitudinal Study of Aging, and the iSTAGING study

¹Artificial Intelligence in Biomedical Imaging Laboratory (AIBIL), Center for and Data Science for Integrated Diagnostics (AI²D), Perelman School of Medicine, University of Pennsylvania, Philadelphia, PA, USA.

²Graduate Group in Applied Mathematics and Computational Science, University of Pennsylvania, Philadelphia, PA, USA.

³Laboratory of AI and Biomedical Science, Stevens Neuroimaging and Informatics Institute, Keck School of Medicine of USC, University of Southern California, Marina del Rey, California, USA.

⁴Laboratory for Research in Neuroimaging, Department of Clinical Neurosciences, Lausanne University Hospital (CHUV) and University of Lausanne, Lausanne, Switzerland

⁵Biggs Alzheimer's Institute, University of Texas San Antonio Health Science Center, USA

⁶The Florey Institute of Neuroscience and Mental Health, The University of Melbourne, Parkville, VIC, Australia

⁷CSIRO Health and Biosecurity, Australian e-Health Research Centre CSIRO, Brisbane, Queensland, Australia

⁸Translational Gerontology Branch, Longitudinal Studies Section, National Institute on Aging, National Institutes of Health, MedStar Harbor Hospital, 3001 S. Hanover Street, Baltimore, MD, USA

⁹Department of Neurology, Johns Hopkins University School of Medicine, Baltimore, MD, USA

¹⁰Wisconsin Alzheimer's Institute, University of Wisconsin School of Medicine and Public Health, Madison, Wisconsin, USA

¹¹Knight Alzheimer Disease Research Center, Washington University in St. Louis, St. Louis, MO, USA

¹²Mallinckrodt Institute of Radiology, Washington University School of Medicine, St. Louis, MO, USA

¹³Department of Neurology, University of Pennsylvania, Philadelphia, PA, USA

¹⁴Department of Biostatistics, Epidemiology and Informatics, University of Pennsylvania, Philadelphia, USA

¹⁵Laboratory of Behavioral Neuroscience, National Institute on Aging, Baltimore, MD, USA

¹⁶Department of Radiology, University of Pennsylvania, Philadelphia, PA, USA

*Corresponding author:

Christos Davatzikos, Ph.D. – Christos.Davatzikos@penmedicine.upenn.edu
3700 Hamilton Walk, 7th Floor, Philadelphia, PA 19104

†Consortium representatives:

the iSTAGING study: Christos Davatzikos, Ph.D. – Christos.Davatzikos@penmedicine.upenn.edu

the Preclinical AD Consortium: Marilyn S. Albert, Ph.D. – malbert9@jhmi.edu

the Baltimore Longitudinal Study of Aging: Susan M. Resnick, Ph.D. – resnicks@mail.nih.gov

the Alzheimer's Disease Neuroimaging Initiative: Michael W. Weiner, M.D. – michael.weiner@ucsf.edu

Abstract

Disease heterogeneity has been a critical challenge for precision diagnosis and treatment, especially in neurologic and neuropsychiatric diseases. Many diseases can display multiple distinct brain phenotypes across individuals, potentially reflecting disease subtypes that can be captured using MRI and machine learning methods. However, biological interpretability and treatment relevance are limited if the derived subtypes are not associated with genetic drivers or susceptibility factors. Herein, we describe Gene-SGAN – a multi-view, weakly-supervised deep clustering method – which dissects disease heterogeneity by jointly considering phenotypic and genetic data, thereby conferring genetic correlations to the disease subtypes and associated endophenotypic signatures. We first validate the generalizability, interpretability, and robustness of Gene-SGAN in semi-synthetic experiments. We then demonstrate its application to real multi-site datasets from 28,858 individuals, deriving subtypes of Alzheimer’s disease and brain endophenotypes associated with hypertension, from MRI and SNP data. Derived brain phenotypes displayed significant differences in neuroanatomical patterns, genetic determinants, biological and clinical biomarkers, indicating potentially distinct underlying neuropathologic processes, genetic drivers, and susceptibility factors. Overall, Gene-SGAN is broadly applicable to disease subtyping and endophenotype discovery, and is herein tested on disease-related, genetically-driven neuroimaging phenotypes.

Main

Neurologic and neuropsychiatric diseases are associated with pathologic processes, which lead to heterogeneous brain changes modified by underlying genetic determinants, as well as lifestyle and environmental factors. Imaging has been a cornerstone of studying the human brain over the past three decades, enabling the observation and measurement of these changes *in vivo*¹, thereby deepening our understanding of how aging and diseases affect brain structure and function. The combination of artificial intelligence (AI) methods and imaging has recently allowed us to transcend the limitations of patient-control comparisons and identify imaging signatures on an individual basis, thereby deriving imaging-AI (iAI) signatures for early disease detection and individualized prognostication²⁻⁴. However, many such iAI signatures have been developed independently of underlying genetic influences, despite the increasing evidence for strong associations between these iAI biomarkers and genetic variants in brain diseases⁵⁻⁸. This has limited their biological interpretability and ability to provide mechanistic insights, as well as their clinical applicability for potential gene-guided therapy and drug discovery⁹.

The heterogeneity of brain diseases and aging poses further challenges in the biological interpretability and clinical utility of these iAI signatures. In particular, multiple co-occurring pathologic processes can simultaneously and jointly affect the brain. For example, amyloid plaques, tau tangles, and medial temporal lobe neurodegeneration are hallmarks of Alzheimer's pathology, whereas cerebrovascular diseases, frequently co-existing with AD, also contribute to cognitive decline and neurodegeneration with distinct but overlapping effects¹⁰. Various commonly obtained imaging measurements such as volumes of brain structures, cortical thickness, or strength of functional networks lack specificity by virtue of being affected by multiple such pathologies. Methods for disentangling such heterogeneity¹¹⁻¹⁵ can enable precision diagnostics and disease subtyping by identifying the type and extent of pathologic processes that actively influence an individual's brain phenotype.

To address these challenges, we developed a deep learning method, Gene-SGAN (Gene-guided weakly-supervised clustering via generative adversarial networks), to model the heterogeneity of disease effects by estimating respective endophenotypic iAI signatures that reside inside the causal pathway from genetic variants to disease symptoms/diagnosis, which may be considered an 'exophenotype.'¹⁶ Critically, by linking imaging phenotypes with genetic factors, Gene-SGAN endorses biologically interpretable *in vivo* measurements of genetically-driven brain changes associated with pathologic processes and diseases, or an 'endophenotype'. Based on the expression of endophenotypic iAI signatures, Gene-SGAN clusters patients into disease subtypes with relatively more homogeneous and genetically associated brain phenotypes. This subtyping aims to contribute to precision diagnostics, patient stratification into clinical trials, and a better understanding of heterogeneous neuropathologic processes giving rise to similar clinical symptoms.

The foundation of our methodology is a deep learning architecture that links imaging and genetic data in a latent space encoding genetically-driven imaging subtypes of brain pathologies. Critically important in our approach is the generative modeling of pathologic processes, such as effects of a disease or a risk factor on brain structure, via a GAN¹⁷ which maps brain measurements from a reference population (healthy controls) to a target population (disease cohort). This generative modeling of pathologic brain change is linked to genetic risk factors for a disease or a

clinical condition. Moreover, clustering in the latent space directly leads to disease subtyping according to these genetically-associated brain phenotypes. Several mechanisms (**Method 1**) regularize this process, thereby enabling the stability, robustness, and interpretability of the derived subtypes.

Although Gene-SGAN is a general methodology, it is herein presented from the perspective of brain aging and dementia by leveraging data from 28,858 individuals from two large studies. In particular, we seek to unravel genetically-linked heterogeneity of neuroanatomical changes in two different populations: 1) patients with clinical AD or non-demented cognitive impairment, termed Mild Cognitive Impairment (MCI); and 2) cognitively normal older adults with hypertension, a known risk factor for cerebrovascular diseases that contributes to dementia¹⁸.

Results

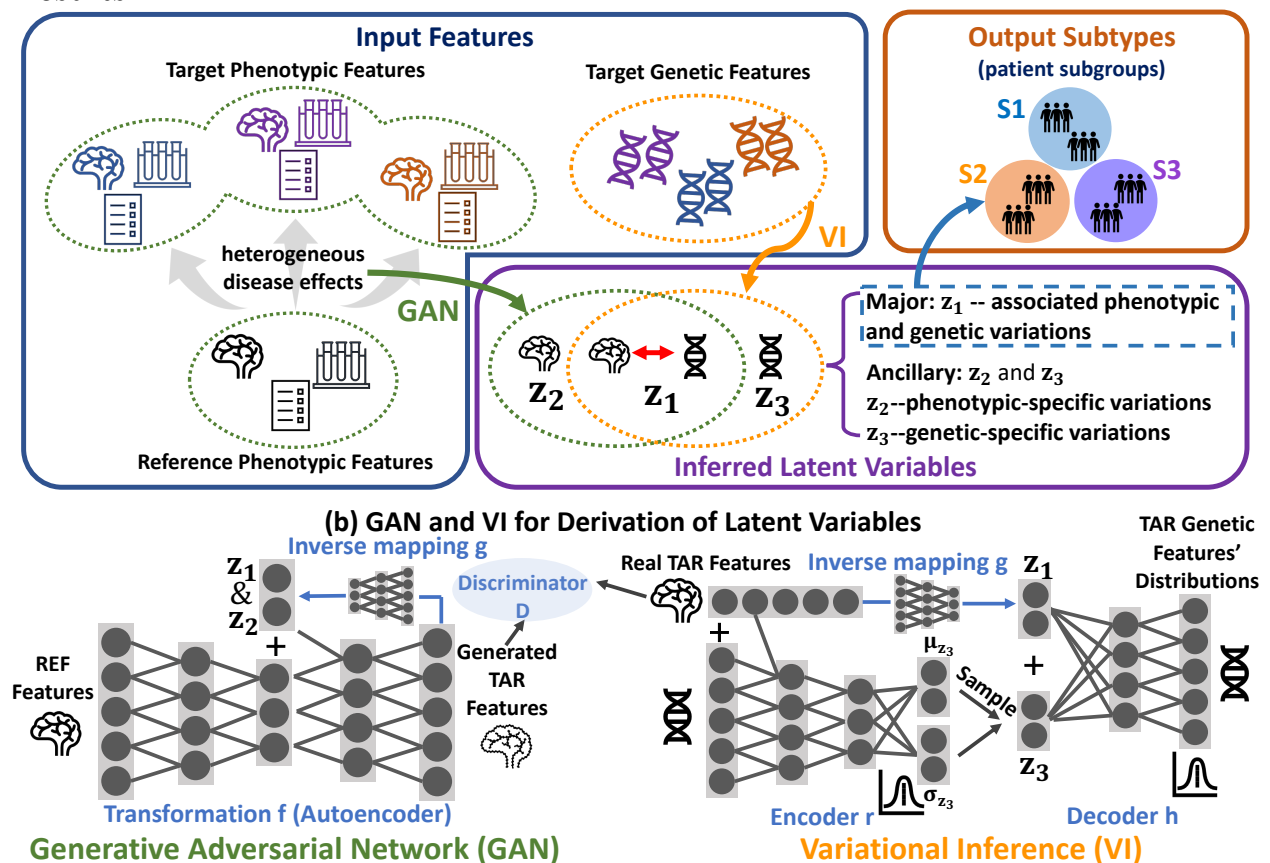


Figure 1. Gene-SGAN identifies disease-related subtypes simultaneously guided by genetic and phenotypic features. *Subtypes*: clusters of patients according to genetically-explained phenotypic variations (e.g., brain neurodegeneration) associated with pathologic processes; *genetic features*: disease-associated genetic factors (e.g., disease-associated SNPs); *phenotypic features*: features from clinical phenotype data, such as imaging features obtained from brain MRI. **(a)** Overview of the Gene-SGAN framework, which aims to identify disease-related subtypes by deriving a group of latent variables z_1 that capture linked phenotypic and genetic variations. To avoid bias in z_1 , two groups of ancillary latent variables, z_2 and z_3 , are learned from the data and capture phenotype-specific and genetic-specific variations, respectively. Particularly, z_1 and z_2 are learned through a GAN that models one-to-many mappings from a reference (REF) group's (e.g., health control (HC) population) to a target (TAR) group's (e.g., patient population) phenotypes, so that they capture disease effects on normal phenotypic features rather than variance affected by disease-unrelated factors such as demographics or disease-unrelated genes. A Variational Inference (VI) approach further encourages the genetic associations of z_1 and z_3 . Taken together, latent variables z_1 , z_2 , and z_3 are

the means by which our approach identifies disease-related subtypes with associated phenotypic patterns and genetic underpinnings. **(b)** GAN and VI are trained iteratively to derive the latent variables. First, to model one-to-many mappings from REF to TAR populations, Gene-SGAN utilizes GAN to learn a transformation function f that generates TAR phenotypic features from REF phenotypic features. As additional inputs of f , the latent variables z_1 and z_2 control the disease-related variations in the generated TAR features (i.e., mapping directions). An inverse mapping g is introduced to re-estimate z_1 and z_2 from the generated TAR features, ensuring that the latent variables characterize sufficiently different and recognizable phenotypic variations. Second, the VI approach estimates the posterior distribution of z_3 (i.e., the mean μ_{z_3} and std σ_{z_3}) based on the TAR phenotypic and genetic features through an encoding neural network r . Simultaneously, through a decoding neural network h , the approach infers the distribution of TAR genetic features conditioned on z_1 and sampled z_3 . Here, z_1 , estimated by the same inverse mapping g in GAN, summarizes necessary information on the TAR phenotypic features for inferring the TAR genetic features' distributions. The plus sign, "+", denotes feature concatenation.

Gene-SGAN: gene-guided weakly-supervised clustering via generative adversarial network to derive disease-related subtypes with distinctive imaging and genetic signatures

Gene-SGAN aims to identify genetically driven disease subtypes from phenotypic and genetic features. In the present work, specifically, we focused on brain phenotypic features derived from magnetic resonance imaging (MRI) and disease-associated single nucleotide polymorphisms (SNPs) as genetic features. The methodological advances of Gene-SGAN are two-fold. First, a deep generative model learns one-to-many mappings from phenotypic measures of a reference population (e.g., brain measurements from healthy controls) to those of a target population (e.g., a patient cohort), thereby capturing the diversity of brain change patterns related to disease. This approach aims to reduce confounders from disease-unrelated variations such as demographic factors or disease-unrelated genetic influences on the brain phenotype. Second, a low-dimensional latent space in Gene-SGAN unravels phenotypic and genetic heterogeneity into latent variables that reflect disease subtypes. In particular, the latent space separately encodes phenotypic subtypes associated with genetic factors through the variables z_1 , while capturing unlinked phenotypic and genetic variations via two ancillary sets of variables z_2 and z_3 , respectively (**Figure 1a**).

Estimation of heterogeneous disease effects on brain phenotypic features. The disease-related one-to-many mappings were constructed via a GAN that learns a transformation function mapping the reference phenotypic features into various types of generated features (**Figure 1b**). The latent variables z_1 and z_2 influence the transformation function and aim to summarize disease-related brain variations among the target populations. As typical in GANs, a discriminator attempts to distinguish the real from the generated disease effects on the brain phenotype, thereby ensuring that the generated brain features follow the distribution of the real target brain features. As a key component of this framework, an inverse mapping is introduced to re-estimate the latent variables z_1 and z_2 from the generated target features so that the latent variables capture distinct and recognizable brain signatures, which contributes to interpretability of respective iAI phenotypes. Estimation of these unknown latent variables with comparison to a reference population is referred to as **weakly-supervised learning** in this study.

Derivation of latent variables with genetic underpinnings. Gene-SGAN also incorporates the genetic features into the model framework to identify disease-related subtypes with genetic underpinnings. Through a Variational Inference (VI) approach (**Figure 1b**), the model approximates the distribution of genetic features based on the latent variables z_1 and z_3 through a decoding neural network. In particular, disease-related phenotypic signatures associated with genetic features are summarized by the variable z_1 , which is estimated by the same inverse mapping incorporated in the GAN training process. Moreover, another encoding neural network

estimates the posterior distribution of the latent variable z_3 that captures the genetic variance not reflected by brain characteristics. Refer to **Method 1** for mathematical details.

Incorporated in the frameworks for both GAN and VI, the M-dimensional categorical variable z_1 is the key latent variable that characterizes disease-related variations induced by phenotypic-genetic associations. The inverse mapping of the trained Gene-SGAN model is applied to participants' phenotypic features only to estimate their latent variables z_1 , which indicate their probabilities belonging to the M subtypes that display genetic associations. Each participant was subsequently assigned to a single subtype based on the maximum probability.

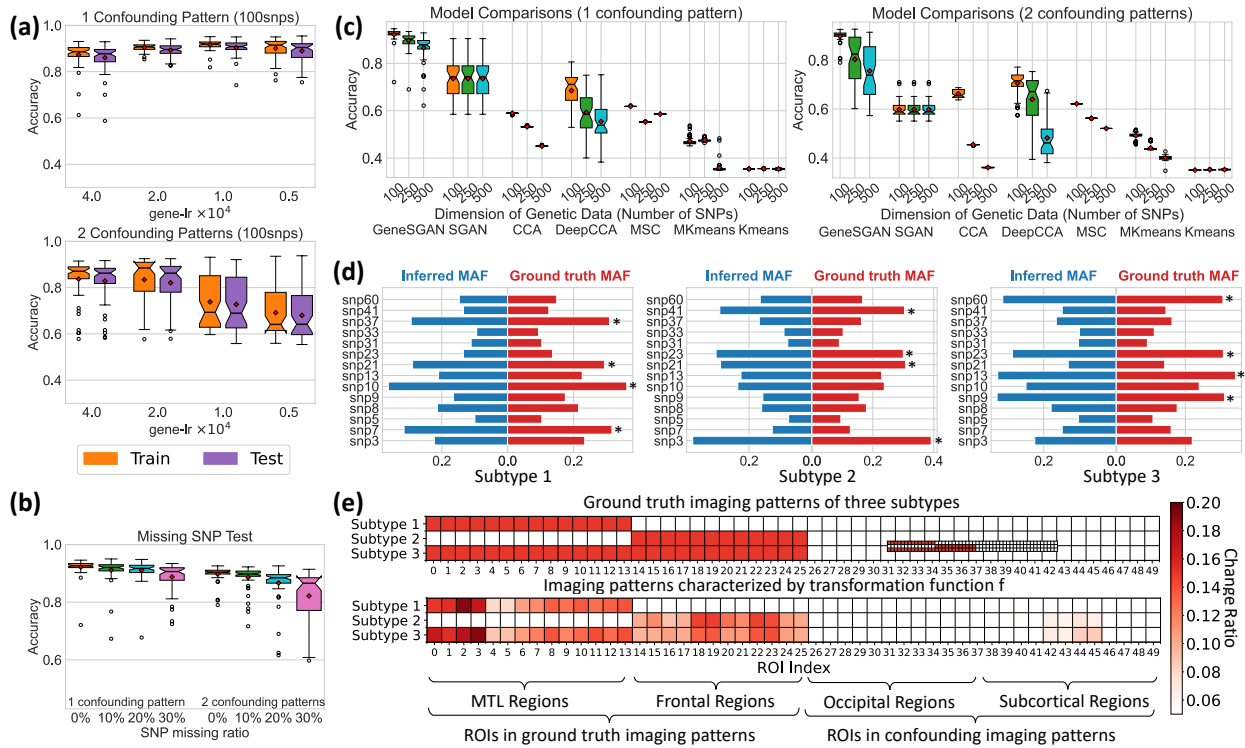


Figure 2. Gene-SGAN identifies the ground truth in semi-synthetic experiments. For constructing different ground truth subtypes, we impose distinct synthesized imaging patterns, specifically volumetric change in brain regions of interest (ROIs), on HC imaging features, simulating disease effects modulated by completely synthetic SNP variations. (**Method 6**). With the known synthetic ground truth, we tested the clustering performance of Gene-SGAN in several experimental scenarios: (a) generalizability to test data, (b) robustness to missing genotype, (c) comparison to previous methods, and (d, e) interpretability for model performances. **a** Gene-SGAN shows robust generalizability to test data. With different hyperparameter ($gene-lr$) settings, Gene-SGAN consistently achieves comparable clustering accuracies on the training and test sets. With increasing confounders in imaging features (bottom vs. top), a higher $gene-lr$ is required to achieve the optimal performance of the model. **b** Gene-SGAN is robust to different levels of missing SNPs. Clustering accuracies remain high but gradually decrease with a higher missing rate of SNPs. **c** Gene-SGAN outperforms other clustering methods. We report the clustering performances of the seven models (Gene-SGAN vs. others) with different levels of simulated imaging confounders and dimensions of genetic data. SGAN: Smile-GAN; CCA: Canonical Correlation Analysis; MSC: Multiview-Spectral-Clustering; MKmeans: Multiview-KMeans. **d** Gene-SGAN accurately recovers SNPs' minor allele frequency (MAF) within each simulated subtype. We present the simulated subtype-associated SNPs (marked with *) and the simulated confounding SNPs (not marked, **Method 6**). **e** Gene-SGAN captures the dominant characteristics of the ground truth imaging patterns (associated with subtypes) but avoids confounding imaging patterns. The ROIs included in the ground truth imaging patterns are colored with a ratio of 0.15, which equals the average ratio of simulated changes that represent the disease effects (ranging from 0-0.3). The ROIs included in the confounding patterns are left blank. Imaging patterns characterized by the model are defined as ratios of ROI changes made by the transformation function that aims to

approximate the disease effects. (**Method 6**) For visualization of important ROIs captured by f, we only color ratios > 0.05. MTL: medial temporal lobe.

Semi-synthetic experiments

We validated the Gene-SGAN model in extensive semi-synthetic experiments, using regions of interest (ROIs) from brain MRI and SNP as input phenotypic and genetic features. Using real HC participant ROI data, we constructed Pseudo-patient (Pseudo-PT) data, which we refer to as semi-synthetic data. Specifically, to construct the ROIs of Pseudo-PT participants, we imposed synthetic volumetric change in a set of predefined ROIs on the real HC participants' ROI measures to simulate disease effects. Simultaneously, we constructed completely synthetic genetic data modulating disease effects by randomly sampling minor allele counts of 100, 250, or 500 simulated SNPs. These Pseudo-PT participants were divided into three ground truth subtypes. Each subtype shared one similar imaging pattern (**Figure 2e**) and had higher minor allele frequencies (MAFs) in four selected SNPs compared to the remaining Pseudo-PT participants (**Figure 2d**). Moreover, we introduced confounding imaging patterns to subsets of Pseudo-PT participants who did not have shared genetic features (**Figure 2e**). Similarly, higher MAFs in confounding SNPs were simulated to subsets of Pseudo-PT participants without shared imaging patterns. In the simulation, we retained disease-unrelated variations in imaging features and provided the known ground truth of simulated imaging patterns, SNPs, and subtypes. More details of data simulation are presented in **Method 6**.

Gene-SGAN is generalizable to test data

The generalizability of Gene-SGAN's performances to test data underpins the reliability of derived subtypes. We evaluated Gene-SGAN's generalizability and examined hyperparameter selections in the semi-synthetic experiments (**Method 6**). To this end, we adopted a 50-repetition holdout cross-validation (CV, 20% for testing) procedure. Gene-SGAN consistently achieved comparable clustering accuracies on the training and test sets, endorsing the robustness of the model's generalizability (**Figure 2a**, **Supplementary eFigure 1**). Furthermore, the hyperparameter (*gene-lr*) impacted the clustering performance. *Gene-lr* regulates the importance of genetic features relative to imaging features in optimization (**Method 1**). With increasing simulated imaging confounders in datasets (from one to two), a higher *gene-lr* (4×10^{-4} vs. 1×10^{-4}) led to the optimal performance, suggesting the reliance on genetic data to guide the clustering solution when many non-genetically related confounding factors play a role (**Figure 2a**).

The optimal *gene-lr* in different cases was selected through the CV procedure with a selection metric, *N-Asso-SNPs* (i.e., the number of significantly associated SNPs in the test set) (**Method 6**). *N-Asso-SNPs* was positively associated with the clustering accuracy (**Supplementary eFigure 1**), thus serving as an appropriate metric for selecting optimal hyperparameters in real data applications.

Gene-SGAN is robust to missing SNPs

Missing data are common in genomics using SNPs. Gene-SGAN was designed to handle missing SNPs as a multivariate learning model. To simulate this situation and test the model's robustness, we randomly replaced 10%, 20%, and 30% SNPs with missing values, and retrained Gene-SGAN fifty times using all semi-synthetic participants with the optimal *gene-lr* selected through the CV procedure (**Method 6**). Gene-SGAN obtained outstanding clustering performance in all cases,

albeit with an expected, gradual drop in clustering performance with an increased missing rate (**Figure 2b**).

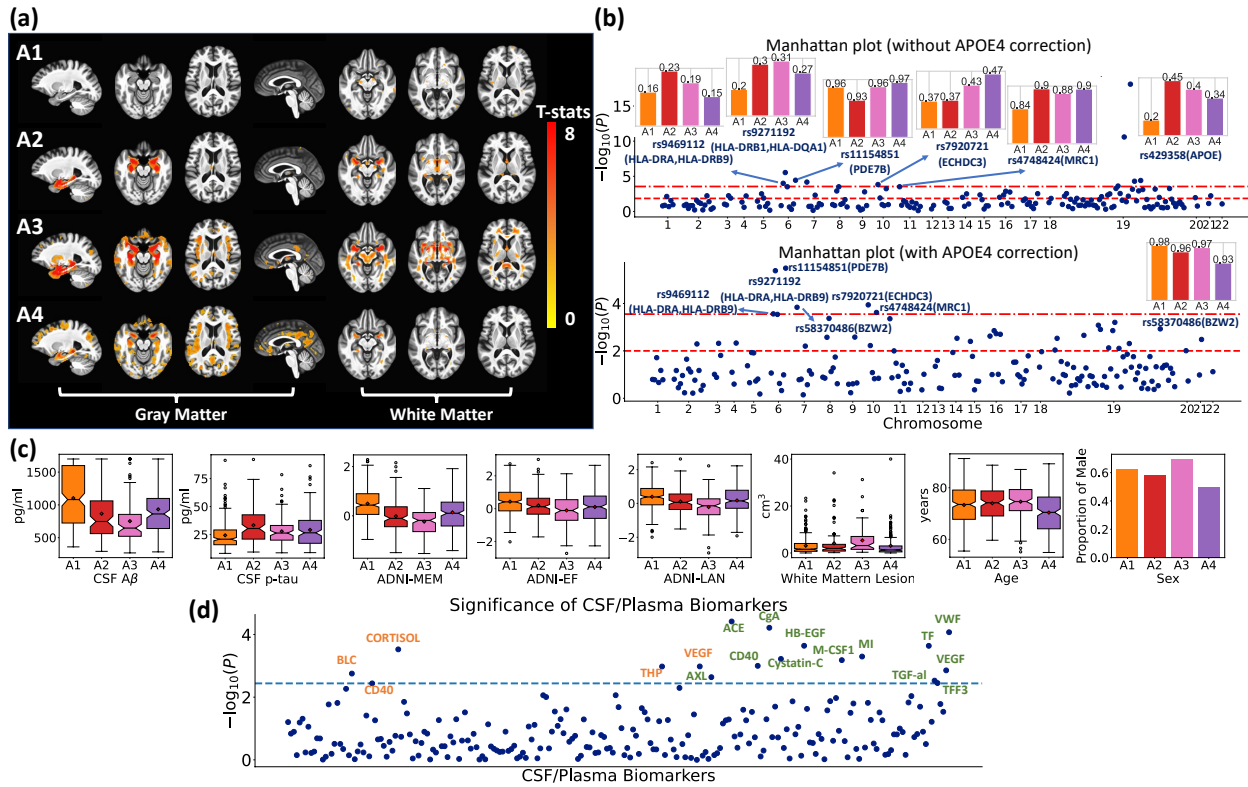
Gene-SGAN outperforms competing methods

With the known ground truth of the simulated subtypes, we compared the clustering performance of Gene-SGAN to six previously proposed methods (**Method 6 and Supplementary eMethod 3**): Smile-GAN model (SGAN, which shares the principal of weakly-supervised clustering with Gene-SGAN)¹¹, Canonical Correlation Analysis (CCA)¹⁹, DeepCCA²⁰, Multiview-Spectral-Clustering (MSC)²¹, Multiview-KMeans (MKmeans)²², and Kmeans²³. We ran each method fifty times using the complete datasets for different simulation cases, defined by varying levels of confounders and dimensions of genetic data. In all cases, Gene-SGAN outperformed these methods in terms of subtype assignment accuracies (**Figure 2c**). The alternative methods were limited because they either could not incorporate genetic data or cluster patient phenotypes directly, which can result in confounding by disease-unrelated variations, such as demographics and disease-unrelated genetic influences on the brain phenotypes. In contrast, Gene-SGAN is not only guided by both imaging and genetic data (multi-omics and multi-view) but also suppresses disease-unrelated confounding variations by effectively modeling mappings from HC to patient populations, which aims to cluster disease effects.

Gene-SGAN accurately estimates simulated disease effects and genetic underpinnings, offering a means for mechanistic interpretations

Gene-SGAN offers a mechanism for interpreting identified subtypes and their related pathological processes. As an example, we utilized the fifty Gene-SGAN models trained for model comparisons on the dataset with 100 candidate SNPs and 2 confounding imaging patterns, leveraging outputs of functions h and f for interpreting the derived subtypes and model performances. (**Method 6**) The function h accurately inferred the simulated genetic distributions (MAFs of SNPs) of subtypes (**Figure 2d**). Moreover, the derived transformation function f recovers the true simulated brain changes due to the subtype-specific disease effects, elucidating the identified iAI signatures corresponding to each subtype. (**Figure 2e**) Therefore, these functions of Gene-SGAN not only explain how the model determines the subtypes but also offer mechanistic insights into how the disease changes brain characteristics via genetically-mediated processes. (**Method 1 and 6**)

Figure 3. Gene-SGAN identifies four subtypes of brain changes related to AD (A1, A2, A3, and A4). a The four subtypes show different imaging patterns compared to HC.



False discovery rate (FDR) correction was performed to adjust multiple comparisons with a p-value threshold of 0.05. Warmer color denotes more brain atrophy in the subtype versus HC. **b** The four subtypes show distinct genetic underpinnings. The Manhattan plots show significant SNP-subtype associations among 178 AD-associated SNPs (likelihood-ratio test with multinomial logistic regression models) with (below) and without (above) adjusting for *APOE* $\epsilon 4$. The two dashed lines denote the p-value thresholds of 0.05 after adjusting for multiple comparisons via Bonferroni (top) and Benjamini-Hochberg (B-H, bottom) methods, respectively. We manually annotated the significant SNPs that survived the Bonferroni correction with the SNP numbers and the mapped genes via their physical positions. We defined the effective allele of each SNP to be the allele positively associated with AD reported in previous literature. EAFs (effective allele frequencies) among each subtype are shown with bar plots. A higher frequency indicates a higher risk of AD. **c** The four subtypes show distinct clinical, cognitive, and demographic characteristics, including CSF $A\beta$ and p-tau (other CSF biomarkers were separately evaluated in **d**). Box and whisker plots and bar plots reveal clinical, demographic, and cognitive variables of MCI participants by subtype. **d** The four subtypes show significant differences in CSF and plasma biomarkers. The Manhattan plots show the significance of differences (ANOVA test) among four subtypes related to AD. The dashed line represents the B-H corrected significance line. Orange-colored names: plasma biomarkers; green-colored names: CSF biomarkers. (Centerline, median; red marker: mean; box limits, upper and lower quartiles; whiskers, 1.5 \times interquartile range; points, outliers).

Subtypes of brain changes associated with AD and genetic variants

We first tested Gene-SGAN in the context of AD using 472 CN, 784 MCI, and 277 clinical AD participants from the ADNI study. We applied the Gene-SGAN model to the 144 imaging ROIs and 178 AD-associated SNPs of these participants, with *M* being set as 3, 4, and 5. Gene-SGAN identified consistent and refined imaging subtypes from a coarse (e.g., *M*=3) to a refined resolution (e.g., *M*=5) (**Supplementary eFigure 2**). We presented the results with *M*=4 because previous studies^{11,14} consistently reported four distinct imaging subtypes in AD. Results for other resolutions of *M* are presented in **Supplementary eFigure 2a** and **Supplementary eData 1**. We denoted the four subtypes related to AD as A1, A2, A3, and A4. Besides subtypes determined by the major latent variable z_1 of Gene-SGAN, we also examined z_2 and z_3 derived on this dataset,

thereby validating their functionality in capturing non-linked imaging-specific and genetic-specific variations. (**Supplementary eFigure 4**)

Subtypes related to AD show distinct imaging signatures

The participants assigned to each subtype showed distinct imaging patterns compared to participants in the cognitively normal HC participants (**Figure 3a**). In voxel-based morphometry analyses, A1 (N=311) exhibited relatively preserved regional brain volumes; A2 (N=197) displayed focal medial temporal lobe (MTL) atrophy, prominent in the hippocampus and the anterior-medial temporal cortex; A3 (N=281) showed widespread brain atrophy over the entire brain, including MTL; A4 (N=272) displayed dominant cortical atrophy with relative sparing of the MTL.

Subtypes related to AD show distinct genetic architectures

We tested SNP-subtype associations among 178 AD-associated SNPs using a likelihood-ratio test on two multinomial logistic regression models fitted with and without each SNP (**Method 8**), adjusting for covariates, including age, sex, *APOE ε4*, intracranial volume (ICV), and the first five genetic principal components. Through the test, we found that four subtypes are significantly different in 5 SNPs after Bonferroni correction ($p=2.81 \times 10^{-4}$), including rs7920721 ($p=1.1 \times 10^{-4}$), rs11154851 ($p=3.2 \times 10^{-6}$), rs9271192 ($p=4.2 \times 10^{-6}$), rs9469112 ($p=2.7 \times 10^{-4}$), and rs4748424 ($p=2.4 \times 10^{-4}$). Without controlling for *APOE ε4* as a covariate, rs429358 ($p=7.8 \times 10^{-19}$) was the most significantly associated SNP – the strongest genetic risk factor in sporadic AD²⁴ (**Figure 3b and Supplementary eData 1**). Detailed differences among subtypes in each SNP are demonstrated in **Figure 3b**, which shows effective allele frequencies (EAF) within each subtype. A higher EAF indicates a higher risk of AD based on previous literature.

The effective incorporation of genetic features in Gene-SGAN significantly boosts the statistical power to detect robust SNP-subtype associations, as demonstrated by the comparison with the SmileGAN model¹¹, which derives four subtypes based on imaging features only using the similar weakly-supervised approach, yet the same test of SNP data within these subtypes does not identify any SNP-subtype associations on the same dataset after adjusting for *APOE ε4*.

Subtypes related to AD show different clinical profiles

The four subtypes differed in age, sex, Aβ/tau measurements, white matter hyperintensity (WMH) volumes, and cognitive performance (**Figure 3c**). Among participants diagnosed as MCI at baseline, A4 participants were the youngest group ($p<0.001$ vs. all other groups) and included more females than A1 and A3 ($p=0.004$ vs. A1 and $p<0.001$ vs. A3). A3 participants had the most abnormal CSF Aβ ($p<0.001$ vs. A1&A4 and $p=0.039$ vs. A2). However, A2 participants showed significantly higher CSF p-tau than A3 participants ($p=0.019$). For cognitive scores, A1 and A3 participants showed the best and the worst performances in memory, executive function, and language. A3-dominant participants also exhibited higher WMH volumes than all other dominant groups ($p<0.001$ vs. A1&A4 and $p=0.017$ vs. A2).

We also characterized the four subtypes with regard to additional 229 plasma and CSF biomarkers. Tested through one-way ANOVA, the four subtypes had significant differences in 18 plasma/CSF biomarkers after adjusting for multiple comparisons via Benjamini-Hochberg (B-H) method (**Figure 3d and Supplementary eData 2**). In contrast, subtypes derived by Smile-GAN do not show significant differences in these biomarkers. The comparison suggests the increased power of Gene-SGAN in identifying subtypes that reflect heterogeneity not only in imaging and

genetic features but also in other clinical biomarkers, implying greater ‘biological relevance’ for these subtypes. For example, among the associated biomarkers, tissue factor (TF) and von Willebrand factor (VWF) are highly expressed at blood-brain barrier^{25,26}, playing important roles in hemostasis; macrophage colony-stimulating factor (MCSF), CD40, chromogranin A (CgA), Cystatin-C contribute to microglial activation or proliferation²⁷⁻³¹; angiotensin-converting enzyme (ACE) and heparin-binding EGF-like growth factor (HB-EGF) are involved in the process of A β degradation and clearance^{32,33}. These results suggest potential biological pathways affected by AD disease mechanisms³⁴⁻³⁶, which could be involved in disease pathogenesis or a direct or indirect response to disease-related neuroanatomical heterogeneity.

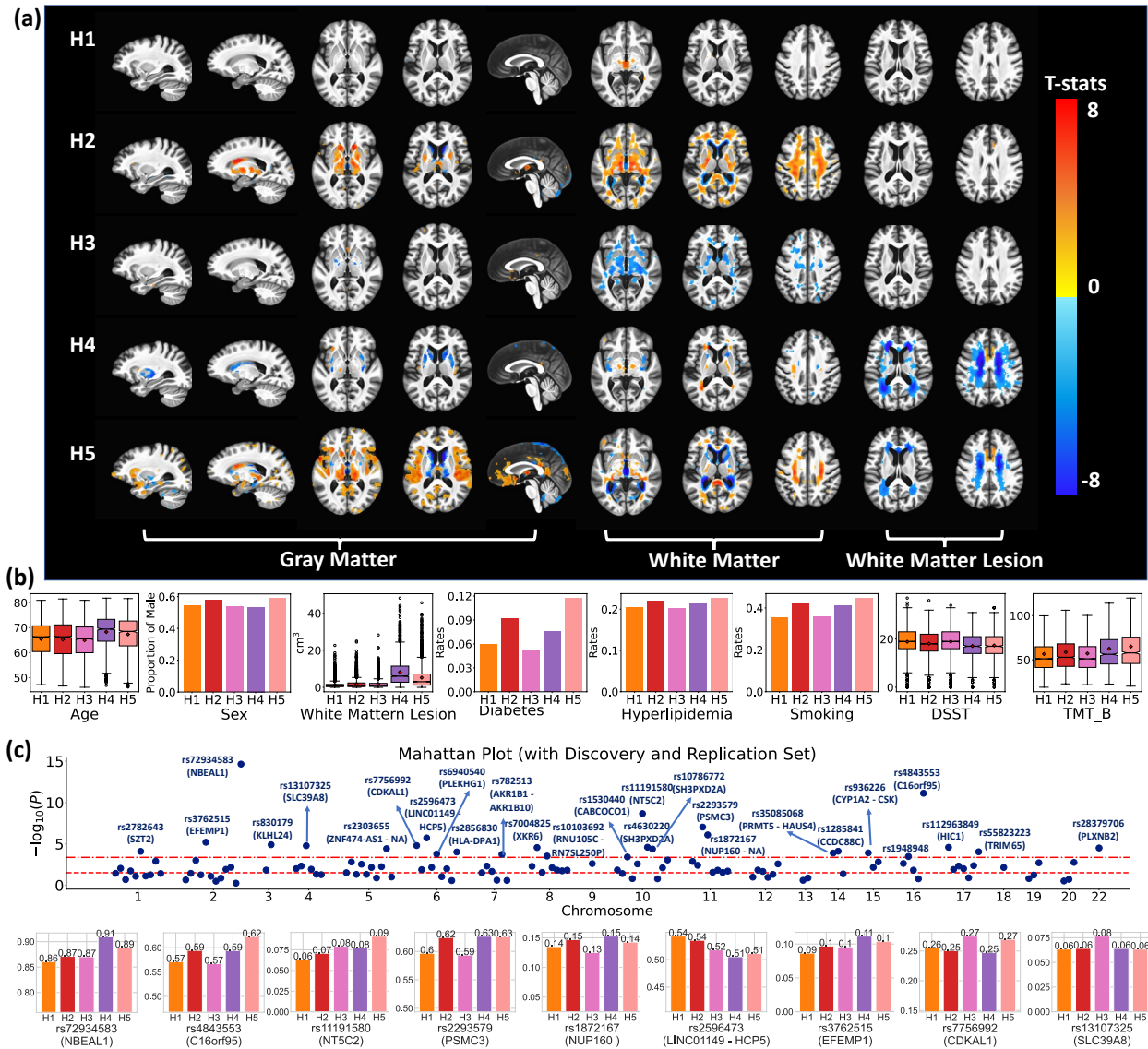


Figure 4. Gene-SGAN identifies five subtypes of brain changes related to hypertension (H1-H5). **a** The five subtypes show distinct imaging patterns. Voxel-wise group comparisons (two-sided t-test) were performed between HC participants (i.e., non-hypertensive participants) and participants assigned to H1, H2, H3, H4, and H5, respectively. False discovery rate (FDR) correction for multiple comparisons with a p-value threshold of 0.05 was applied. Warmer color denotes brain atrophy (i.e., HC > subtype), and cooler color represents larger tissue volume (i.e., subtype > HC). **b** The five subtypes show distinct clinical, cognitive, and demographic characteristics. Box and whisker plots and bar plots show the characteristic of demographic, clinical, and cognitive variables. In TMT B plots, outliers are excluded

for visualization purposes. (center line, median; red marker: mean; box limits, upper and lower quartiles; whiskers, 1.5× interquartile range; points, outliers). **c** The five subtypes show different genetic architectures. The Manhattan plot displays significant SNP-subtype associations among 117 hypertension-associated SNPs using all hypertensive patients' data. The two dashed lines denote the p-value thresholds of 0.05 after adjusting for multiple comparisons via Bonferroni (top) and B-H methods (bottom). We manually annotated significant SNPs that survived the Bonferroni correction with the SNP numbers and the mapped genes via their physical positions. In this figure, we defined the effective allele of each SNP as the allele positively associated with hypertension or WMH (SNPs identified in hypertension-gene interaction analyses³⁷) reported in previous literature. The bar plots reveal EAFs of the top nine significant SNPs within each subtype.

Subtypes of brain changes associated with hypertension and genetic variants

In our second set of experiments with real data, we tested Gene-SGAN in the context of hypertension using 10,911 non-hypertensive and 16,414 hypertensive participants from the UKBB study. (**Method 7**) Hypertension has been a well-established risk factor for cerebrovascular diseases that contribute to dementia¹⁸ via multiple potential processes, including atherosclerosis, small vessel ischemic disease, inflammation, and blood-brain barrier compromise. We used 144 imaging ROIs, total WMH volumes, and 117 hypertension-associated SNPs as features to train the model, with M being set as 3, 4, and 5. Gene-SGAN identified consistent and refined imaging subtypes from a coarse (e.g., M=3) to a refined resolution (e.g., M=5) (**Supplementary eFigure 3**). We denoted the five subtypes of brain changes associated with hypertension: H1, H2, H3, H4, and H5. Results for other resolutions of subtypes are presented in **Supplementary eFigure 3a and Supplementary eData 3**.

Subtypes related to hypertension show distinct imaging signatures

Participants assigned to each subtype showed distinct imaging patterns compared to HC, non-hypertensive participants (**Figure 4a**). H1 (N=4652) participants showed mild atrophy in the midbrain. H2 participants (N=3543) exhibited severe atrophy in subcortical gray matter (GM) regions as well as other white matter (WM) regions. H3 participants (N=5044) showed larger volumes in deep structures of WM compared to HC. H4 participants (N=1341) showed mild atrophy in cortical and WM regions, as well as larger putamen, caudate, and higher WMH volumes. Finally, H5 (N=1834) participants displayed widespread cortical atrophy in GM and WM with higher WMH volumes.

Subtypes related to hypertension show distinct genetic architectures

We first tested SNP-subtype associations among 117 hypertension-associated SNPs and 5 subtypes using all available hypertensive patient data (N=16,414). 27 SNPs were identified to be significantly different among subtypes after Bonferroni correction for multiple comparisons (**Figure 4c and Supplementary eData 3**). We further performed split-sampled analyses (**Method 7 and Supplementary eMethod 4**) to test the replicability rate of the SNP-subtype associations in two independent splits. Specifically, we equally split the patient data into the discovery set (N=8207) and the replication set (N=8207). Using the discovery set, we re-derived 5 subtypes related to hypertension using Gene-SGAN and further found 15 significant SNP-subtype associations (**Method 8**) after Bonferroni correction. Among these, 10 SNP-subtype associations (66.7%) were replicated in the replication set at B-H corrected significance, and 7 (46.7%) were significant after Bonferroni corrections for multiple comparisons (**Supplementary eMethod 4**).

In contrast, we found only 5 SNPs significantly associated with Smile-GAN subtypes in the discovery set. Among them, only 1 SNP was replicated in the replication set at both B-H corrected and Bonferroni corrected significance (**Supplementary eData 5**). Details of the

reproduced SNPs are presented in **Supplementary eData 4**. These results further support the increased power of Gene-SGAN in GWAS.

Subtypes related to hypertension show distinct clinical profiles

We examined the clinical profiles of the five subtypes with regard to demographics, comorbidities, and cognitive scores (**Figure 4b**). WMH volumes were the highest among H4 participants ($p < 0.001$ vs. all other H) and the second highest among H5 participants ($p < 0.001$ vs. H1-H3). In terms of comorbidities, H5 participants had significantly higher rates of diabetes ($p < 0.001$ vs. H1, H3, H4, and $p = 0.004$ vs. H2), while H2 and H4 participants also displayed significantly higher rates of diabetes than H1 and H3 participants ($p < 0.001$ for H2 vs. H1&H3, $p = 0.039$ for H4 vs. H1, and $p = 0.001$ for H4 vs. H3). The five subtypes did not exhibit significant differences in hyperlipidemia. H1 and H3 participants had a significantly smaller proportion of smokers ($P < 0.001$ vs. all other groups). In cognition, H4 and H5 participants showed the worst performance as measured by DSST and TMT-B ($p < 0.001$ vs. H1-H3 in three scores), while H2 participants showed worse performance than H1 and H3 participants ($p < 0.001$ in DSST and TMT-B).

Discussion

In the current work, we proposed Gene-SGAN – a novel deep weakly-supervised clustering method – to unravel disease heterogeneity and develop genetically-explained disease subtypes having distinct brain phenotypes. The novelty of Gene-SGAN lies in its multi-view modeling nature, which ensures that the derived disease subtypes not only reflect distinct neuroanatomical patterns but are also associated with underlying genetic determinants. The following two central points bolster the advantage of Gene-SGAN over other clustering methods^{11,19-23}. First, through the generative and weakly-supervised modeling of disease heterogeneity, Gene-SGAN seeks to cluster based on disease-related variations in phenotypic data, achieved via clustering of transformations of brain phenotypes, which helps avoid confounding variations associated with demographic and disease-irrelevant genetic factors. Second, Gene-SGAN links phenotypic and genetic variations through three sets of latent variables, which separately encode linked and non-linked genetic and phenotypic variations, thereby enabling the identification of unbiased phenotypic subtypes with genetic associations. Through extensive and systematic semi-synthetic and real data experiments, we demonstrated the efficacy and applicability of Gene-SGAN in deriving biologically and clinically distinct disease subtypes.

Our experiments focused on applying Gene-SGAN to imaging features from brain MRIs and SNPs. However, Gene-SGAN is widely applicable to other multi-omics biomedical data, including various sources of phenotypic (e.g., other clinical variables) and genetic features (e.g., gene expression data). Specifically, with preselected reference populations and genetic features, Gene-SGAN can effectively discover genetically driven subtypes of phenotypic features related to various diseases or disorders. Moreover, commonly observed missing genotypes limit the applicability of many multivariate methods that require dropping participants with missing features. In contrast, Gene-SGAN is robust to missing genotypes and optimally models disease heterogeneity with all available genetic features. This property is essential in imaging genomics studies, which often suffer from relatively small sample sizes due to the difficulty in data collection. The high tolerance and sophisticated adoption of missing data enable Gene-SGAN to be a general method for modeling disease heterogeneity in biomedical studies. In our experiments, we demonstrated the robust applicability of Gene-SGAN by applying it to two independent datasets for studying two distinct pathologies: AD and hypertension. The method effectively discovers genetically and neuroanatomically driven subtypes in AD/MCI and hypertension, yielding increased statistical power for downstream statistical analyses.

Gene-SGAN identified four AD-related subtypes with distinct characteristics. A1 is characterized by preserved brain volume with the lowest levels of cognitive impairment and A β /tau deposition, indicating a resilient subtype. A2 is associated with focal MTL atrophy and high CSF-tau, suggesting a subtype driven by limbic-predominant, likely rapidly progressive neuropathology (high tau levels, despite the localized nature of neurodegeneration). A3 is characterized by severe atrophy in cortical and MTL regions, the most abnormal CSF-A β , the worst cognitive performances, and the highest WMH volumes. Patients assigned to this subtype might mainly have a manifestation of typical AD pathology as well as vascular co-pathology. A4 participants exhibit severe cortical but relatively modest MTL atrophy patterns, indicating a mixture of participants with a cortical presentation of AD and those with other neural degenerative processes (e.g., advanced brain aging⁴). A significantly lower age range of A4 participants suggests the inclusion of EOAD participants, who were characterized by hippocampal-sparing disease with

posterior cortical atrophy³⁸. Notably, the four subtypes were significantly associated with known AD-related genetic variants. Among all subtype-associated SNPs, rs429358 in the *APOE* gene was the strongest genetic risk factor for sporadic AD²⁴ and was associated with hippocampal atrophy and cognitive decline^{39,40}. Two other SNPs (rs9469112 and rs9271192) were mapped to the HLA region that was involved in immune response modulation⁴¹⁻⁴³. Our results showed a lower frequency of EAFs of these three SNPs among A1 participants, indicating a protective effect contributing to the observed resilience. In contrast, the highest EAFs of rs429358 and significant MTL atrophy of A2 participants resemble the previously reported characteristics of limbic-predominant AD⁴⁴. Higher EAFs in rs9469112 and rs9271192 in A2 and A3 suggest the potential for inflammatory mechanisms contributing to these two subtypes. A4 participants have the highest EAF in rs7920721, an SNP exclusively associated with AD among participants who don't carry *APOE* ϵ ⁴⁵. Our A4 subtype supports this finding while further linking the effect of this SNP with an atypical atrophy pattern of AD, likely accompanied by co-pathologies. Critically, compared to AD-related subtypes derived with imaging features only, these four subtypes possess more significant differences in a large set of plasma/CSF biomarkers, which are related to distinct biological mechanisms contributing to the heterogeneity of AD. Taken together, the four AD-related subtypes identified by Gene-SGAN support the conclusion that disease heterogeneity modeling with genetic guidance better reflects upstream biological processes and boosts downstream analyses' statistical power.

Gene-SGAN identified five clinically distinct hypertension-related subtypes, which reflect the remarkable heterogeneity of the effects of hypertension on brain structure. The H1 and H3 participants exhibit the best cognitive performances and lowest rates of comorbidities. Though sharing similarities in preserved GM volumes, these subtypes differ in WM structures. The H2 subtype is characterized by subcortical and WM atrophy, with a higher rate of diabetic participants. Previous studies have reported hypertension-related influence on subcortical morphology⁴⁶ and WM integrity^{47,48}. However, WM microstructures of these subtypes need to be further explored through diffusion MRI. Both the H4 and H5 subtypes are associated with high WMH volumes, the most commonly used biomarker of cerebral small vessel ischemic disease, and worse cognitive performances. In addition, a higher rate of diabetes is observed among H5 participants, which partially explains the widespread atrophy patterns associated with the H5 subtype based on previous studies^{49,50}. These five subtypes not only resemble the previously reported associations among blood pressure, comorbidities, and neuroanatomical changes⁴⁷⁻⁵³, but also further dissect variations in brain changes, potentially elucidating heterogeneous effects from various underlying hypertension-related or hypertension-inducing pathological processes. Among subtype-associated SNPs, rs72934583, rs4843553, and rs3762515 were previously associated with WMH volumes³⁷, which are consistent with their higher EAFs among H4 and H5 participants in our findings. rs11191580, rs7756992, and rs13107325 were linked in previous GWAS to diabetes and obesity⁵⁴⁻⁵⁷, two comorbidities of hypertension.

We demonstrated the generalizability of Gene-SGAN clustering through cross-validation and independent replication. The reproducibility crisis⁵⁸ has drawn much attention in machine learning and casts a shadow over future clinical translation. For genetic studies, replication of associations also underpins the reliability of discovered genetic variants with modest effect sizes⁵⁹. First, extensive cross-validated experiments on semi-synthetic datasets supported the generalizability of Gene-SGAN's performance to unseen data in identifying simulated subtypes.

Furthermore, we validated Gene-SGAN's ability to identify subtypes with reproducible genetic associations on real datasets through split-sampled experiments on the hypertensive population. Several methodological considerations ensure the reproducibility of Gene-SGAN subtypes. For example, the incorporation of ancillary latent variables (e.g., z_2 and z_3) and sparse transformations implicitly regularized SNP-subtype associations identified in the discovery set. The ensemble learning procedure for deriving the final subtypes (e.g., the consensus of models derived through hold-out CV) further encouraged the replicability of SNP-subtype associations. In conclusion, Gene-SGAN can derive reproducible subtypes that are also biologically and genetically interpretable.

The potential clinical impact of Gene-SGAN is versatile; clustering of individuals into clinically meaningful disease subtypes has important implications and applicability. First, deriving robust disease-related subtypes may help improve classification performance for individualized disease diagnosis and prognosis. Second, modeling disease heterogeneity provides new patient stratification and treatment evaluation tools for future clinical trials, which remain important in the setting of mixed results and clinical limitations of anti-amyloid treatments. Our results suggest that disease subtyping via Gene-SGAN could reveal more significant imaging and genomic characteristics which are compromised in case-control comparisons due to the underlying heterogeneity. Third, Gene-SGAN subtypes are genetically relevant by modeling, which serves as a reliable endophenotype to pinpoint potential causal genetic variants for drug repurposing and discovery.

There are potential improvements to the current study. First, the MCI/AD subtypes were derived from a relatively modest sample size ($N=1061$). Ongoing efforts, including the unprecedented consolidation of large-scale imaging-genomic consortia of AD, such as the AI4AD consortium (<http://ai4ad.org/>), may provide opportunities to produce more reproducible and diverse disease subtypes, including less common genetic-structural patterns. Second, in this study, we validated the performance of Gene-SGAN using candidate SNPs directly associated with the disease of interest. For future applications of Gene-SGAN, it might deserve to try different SNP selection criteria that restrict or relax the scope of candidate SNPs. For instance, we could incorporate SNPs based on information from druggable genes⁶⁰, thereby providing more insights into drug discoveries.

In summary, Gene-SGAN effectively unravels phenotypic variations driven by genetic factors into multiple disease-related subtypes to comprehensively understand disease heterogeneity. Gene-SGAN can be widely and easily applied to biomedical data from different sources to derive clinically meaningful disease subtypes. These iAI subtypes provide great potential for drug discovery and repurposing, optimization of clinical trial recruitment, and personalized medicine based on an individual's genetic profile.

Methods

Method 1. The Gene-SGAN model

Gene-SGAN is a multi-view, deep weakly-supervised clustering method based on GAN and variational inference (VI). Gene-SGAN aims to cluster patients from varying sources of phenotypic (e.g., clinical variables or imaging features derived from MRI) and genetic features (e.g., SNP). For this purpose, the model learns three sets of latent variables. The M -dimensional categorical variable, comprising the vector z_1 , captures joint genetic and phenotypic variations and indicates the probabilities of M output clusters, referred to as subtypes. Two ancillary sets of variables, comprising the vectors z_2 and z_3 , summarize phenotypic-specific and genetic-specific variations, respectively. Critically, the model avoids confounders from disease-unrelated variations in phenotypic features under the framework of weakly-supervised clustering⁶¹. To sum up, Gene-SGAN employs a GAN generative model to construct one-to-many mappings from a reference population (i.e., HC) to a target population (i.e., patient) instead of clustering based on global similarity/dissimilarity in the patient population, which might be affected by demographics, lifestyle, or disease-unrelated genetic influences. In addition, VI is used to ensure that disease-related genetic features jointly guide the clustering solution. The framework of Gene-SGAN (**Figure 1b**) consists of two main optimization steps: the **Phenotype step** (via GAN) and the **Gene step** (via VI), as detailed below.

For conciseness, we denote the following variables: x : the REF phenotypic features; y : the TAR phenotypic features; y' : the synthesized TAR phenotypic features; v : the genetic features; z_1, z_2, z_3 : the three latent variables in Gene-SGAN. The distributions of these variables are denoted as: $x \sim p_{\text{ref}}(x)$, $y \sim p_{\text{tar}}(y)$, $y' \sim p_{\text{syn}}(y')$, $z_1 \sim p_{\theta_{z_1}}(z_1)$, $z_2 \sim p_{z_2}(z_2)$, $z_3 \sim p_{z_3}(z_3)$, where $p_{\theta_{z_1}}(z_1)$ is a parametrized distribution updated during the training procedure. In addition, $\theta_D, \theta_f, \theta_g, \theta_h, \theta_r$, represent parameters of the five parametrized functions (**Figure 1b**).

Phenotype step. The Phenotype step incorporates only the phenotypic features for optimization. Gene-SGAN learns one transformation function, $f: X \times Z_1 \times Z_2 \rightarrow Y$, that maps REF features x to different synthesized TAR features $y' = f(x, z_1, z_2)$, with the latent variables z_1, z_2 specifying variations in the synthesized features (i.e., different mapping directions). Specifically, z_1 contributes to phenotypic variations with genetic associations. In contrast, z_2 contributes to phenotype-specific variations without genetic associations. The latent variable, $z_2 \sim p_{z_2}(z_2)$, is sampled from a predefined multivariate uniform distribution $U[0,1]^{n_{z_2}}$ with the dimension n_{z_2} ; $z_1 \sim p_{\theta_{z_1}}(z_1)$ follows an M -dimensional categorical distribution (i.e., an M -dimensional one-hot vector) parametrized by θ_{z_1} (i.e., probabilities of categories). This enables the model to derive robust clustering solutions with imbalanced cluster sizes. An adversarial discriminator D is introduced to distinguish between the real TAR features y and the synthesized TAR features y' , thereby ensuring that the synthesized TAR features from f are indistinguishable from the real TAR features. Moreover, we introduce three types of regularization to encourage that the transformation function approximates underlying pathological processes: the sparse transformation, the Lipschitz continuity, and the inverse consistency. The complete objective function of the Phenotype step is thus a combination of the adversarial loss and the regularization terms, as detailed below.

First, we modify the adversarial loss of the basic GAN and the Smile-GAN model to update the distribution of the latent variable $z_1 \sim p_{\theta_{z_1}}(z_1)$, so that the clustering model is robust to

imbalanced data. Details of this modification are presented in **Supplementary eMethod 1.2**. The modified adversarial loss is written as:

$$\begin{aligned}
L_{\text{GAN}}(\theta_D, \theta_f, \theta_{z_1}) &= E_{y \sim p_{\text{tar}}(y)} [\log(D(y))] + E_{y' \sim p_{\text{syn}}(y')} [1 - \log(D(y'))] \\
&\quad + \kappa D_{\text{KL}}(p_U(z_1) | p_{\theta_{z_1}}(z_1)) \\
&= E_{z_1 \sim p_{\theta_{z_1}}(z_1), y \sim p_{\text{tar}}(y)} [\log(D(y))] \\
&\quad + E_{z_1 \sim p_{\theta_{z_1}}(z_1), z_2 \sim p_{z_2}(z_2), x \sim p_{\text{ref}}(x)} [1 - \log(D(f(x, z_1, z_2)))] + \kappa D_{\text{KL}}(p_U(z_1) | p_{\theta_{z_1}}(z_1)) \\
&= M * E_{y \sim p_{\text{tar}}, z_1 \sim p_U(z_1)} [p_{\theta_{z_1}}(z_1) \log(D(y))] \\
&\quad + M * E_{z_1 \sim p_U(z_1), z_2 \sim p_{z_2}(z_2), x \sim p_{\text{ref}}(x)} [p_{\theta_{z_1}}(z_1) (1 - \log(D(f(x, z_1, z_2))))] \\
&\quad \quad + \kappa D_{\text{KL}}(p_U(z_1) | p_{\theta_{z_1}}(z_1))
\end{aligned}$$

Intuitively, we sample z_1 from a discrete uniform distribution, $p_U(z_1)$, but penalize the losses with its probability under the distribution $p_{\theta_{z_1}}(z_1)$. The modified loss function enables z_1 to be implicitly sampled from the parameterized distribution $p_{\theta_{z_1}}(z_1)$. $p_{\theta_{z_1}}(z_1)$ is controlled to be not far away from $p_U(z_1)$. Both θ_f and θ_{z_1} are optimized so that the synthesized TAR features follow similar distributions as the real TAR features. The discriminator D provides a probability – y comes from the real features rather than the generator – and aims to distinguish the synthesized TAR features from the real TAR features. Therefore, the discriminator attempts to maximize the adversarial loss function while θ_f and θ_{z_1} are updated to minimize it. The corresponding training process can be denoted as:

$$\begin{aligned}
\min_{\theta_f, \theta_{z_1}} \max_{\theta_D} L_{\text{GAN}}(\theta_D, \theta_f, \theta_{z_1}) &= E_{y \sim p_{\text{tar}}(y)} [\log(D(y))] + E_{y' \sim p_{\text{syn}}(y')} [1 - \log(D(y'))] \\
&\quad + \kappa D_{\text{KL}}(p_U(z_1) | p_{\theta_{z_1}}(z_1))
\end{aligned}$$

Second, we assume that disease-related processes primarily affect a subset of phenotypic features (i.e., sparsity). We, therefore, define a change loss to be the l_1 distance between the synthesized TAR features and the REF features to boost sparse transformations:

$$L_{\text{change}}(\theta_f) = E_{x \sim p_{\text{ref}}(x), z_1 \sim p_U(z_1), z_2 \sim p_{z_2}(z_2)} [\|f(x, z_1, z_2) - x\|_1]$$

Third, the inverse consistency is accomplished by introducing an inverse mapping function g for re-estimating z_1 and z_2 from the synthesized TAR features $f(x, z_1, z_2)$. For clarity in description, we define g_1 and g_2 as two inverse mapping functions that re-estimate z_1 and z_2 , respectively, though they share the same encoding neural network. The cross-entropy loss is used for reconstructing the categorical variable z_1 . While the l_2 loss is used for the continuous variable z_2 . By denoting l_c to be the cross-entropy loss with $l_c(a, b) = -\sum_{i=1}^k a^i \log b^i$, we define the reconstruction loss as:

$$\begin{aligned}
L_{\text{recons}}(\theta_f, \theta_{g_1}, \theta_{g_2}) &= E_{x \sim p_{\text{ref}}(x), z_1 \sim p_U(z_1), z_2 \sim p_{z_2}(z_2)} [l_c(z_1, g_1(f(x, z_1, z_2)))] \\
&\quad + E_{x \sim p_{\text{ref}}(x), z_1 \sim p_U(z_1), z_2 \sim p_{z_2}(z_2)} [\|g_2(f(x, z_1, z_2)) - z_2\|_2]
\end{aligned}$$

The minimization of the reconstruction loss enables the transformation function, f , to identify sufficiently distinct features in the TAR domain depending on the latent variables, z_1 and z_2 .¹¹ Moreover, the inverse function g_1 is critical in the model framework. First, it is optimized in the Gene step (detailed below) for inferring the distributions of the genetic features, thereby allowing the clustering solutions to be genetically guided. Moreover, it serves as a **clustering function** after training to estimate z_1 from real TAR phenotypic features, deriving the probabilities of the cluster memberships (i.e., subtypes). More details of the inverse functions are stated at the end of this section and in **Supplementary eMethod 1.1**.

Lipschitz continuities of the functions f , g_1 , g_2 are ensured through weight clipping as described in **Supplementary eMethod 2.2** instead of through additional loss functions. Therefore, the full objective of the Phenotype step can be written as:

$$L_{\text{Phenotype}}(\theta_D, \theta_f, \theta_{g_1}, \theta_{g_2}, \theta_{z_1}) = L_{\text{GAN}}(\theta_D, \theta_f, \theta_{z_1}) + \mu L_{\text{change}}(\theta_f) + \lambda L_{\text{recons}}(\theta_f, \theta_{g_1}, \theta_{g_2})$$

where μ and λ are two hyperparameters that control the relative importance of each loss function during the training process. Through this objective, we aim to derive parameters, $\theta_D, \theta_f, \theta_{g_1}, \theta_{g_2}, \theta_{z_1}$, such that:

$$\theta_D, \theta_f, \theta_{g_1}, \theta_{g_2}, \theta_{z_1} = \arg \min_{\theta_f, \theta_{g_1}, \theta_{g_2}, \theta_{z_1}} \max_{\theta_D} L_{\text{Phenotype}}(\theta_D, \theta_f, \theta_{g_1}, \theta_{g_2}, \theta_{z_1})$$

Gene step. The Gene step encourages that the clustering solution is associated with genetic features. Specifically, the model learns a parametrized distribution of the genetic features v , conditioned on the phenotypic features y and a new latent variable z_3 , $p_{\theta_h, \theta_{g_1}}(v|z_3, y)$, where z_3 characterizes genetic-specific variations unrelated to the phenotypic features. This is accomplished through the VI method for approximating an intractable posterior distribution, $p_{\theta_h, \theta_{g_1}}(z_3|v, y)$ by a variational distribution $q_{\theta_r}(z_3|v, y)$. From the KL divergence between $p_{\theta_h, \theta_{g_1}}(z_3|v, y)$ and $q_{\theta_r}(z_3|v, y)$, we can derive the evidence lower bound (ELBO) for $p(v|y)$. The derivation is presented in **Supplementary eMethod 1.3**.

$$\log p(v|y) \geq E_{z_3 \sim q_{\theta_r}(z_3|v, y)} [\log p_{\theta_h, \theta_{g_1}}(v|z_3, y) + \log \frac{p_{z_3}(z_3)}{q_{\theta_r}(z_3|v, y)}]$$

The conditional distribution $p_{\theta_h, \theta_{g_1}}(v|z_3, y)$, is parametrized by the functions h and g_1 . Based on different sources of genetic features, it can be modeled as different types of distributions. For instance, herein, we use SNPs as genetic features. We define $p_{\theta_h, \theta_{g_1}}(v|z_3, y) = B(2, p_{\text{binom}}^{\text{genetic}})$ as a multivariate binomial distribution, which has the number of trials equaling two and the dimension equaling the number of SNPs (n_{genetic}). The function h takes z_3 and $g_1(y)$ as inputs and outputs parameters of the conditional distribution, $p_{\theta_h, \theta_{g_1}}(v|z_3, y)$ (e.g., the parameters, $p_{\text{binom}}^{\text{genetic}}$, represent MAFs of SNPs when using SNPs as features). The variational distribution, $q_{\theta_r}(z_3|v, y) = N(\mu^{z_3}, \sigma^{z_3})$, parametrized by a function r , is modeled as a multivariate normal distribution with the dimension equaling n_{z_3} . The function r takes v and y as inputs and outputs μ and σ for each dimension of z_3 . The prior distribution of z_3 , $p_{z_3}(z_3) = N(0^{n_{z_3}}, 1^{n_{z_3}})$, is defined as a multivariate standard distribution. In the Gene step, we maximize the ELBO for $p(v|y)$ by minimizing the following function:

$$-\mathbb{E}_{z_3 \sim q_{\theta_r}(z_3|v, y)} \left[\log p_{\theta_h, \theta_{g_1}}(v|z_3, y) + \log \frac{p_{z_3}(z_3)}{q_{\theta_r}(z_3|v, y)} \right]$$

In the case of missing genetic features, we substitute the missing features with the mean value over observed features among the target population (e.g., two times MAF within the target population for SNP data) and use the imputed genetic features, v^{impute} , as the inputs for the function r . The conditional distribution, $p_{\theta_h, \theta_{g_1}}(v|z_3, y)$, in ELBO is computed with only the observed genetic features v^{observe} ⁶². Therefore, the objective function of the Gene step is written as:

$$L_{\text{Gene}}(\theta_h, \theta_{g_1}, \theta_r) = -\mathbb{E}_{z_3 \sim q_{\theta_r}(z_3|v^{\text{impute}}, y)} \left[\log p_{\theta_h, \theta_{g_1}}(v^{\text{observe}}|z_3, y) + \log \frac{p_{z_3}(z_3)}{q_{\theta_r}(z_3|v^{\text{impute}}, y)} \right]$$

Through this objective function, we derive $\theta_h, \theta_{g_1}, \theta_r$ such that

$$\theta_h, \theta_{g_1}, \theta_r = \arg \min_{\theta_h, \theta_{g_1}, \theta_r} L_{\text{Gene}}(\theta_h, \theta_{g_1}, \theta_r)$$

Notably, the term, $\log \frac{p_{z_3}(z_3)}{q_{\theta_r}(z_3|v^{\text{impute}}, y)}$, can also be considered a regularization term. Through regularization, we control the contribution of z_3 in the inference of genetic distributions and thus guarantee the contribution from the phenotypic features y .

The Phenotype and Gene optimization steps are performed iteratively during the training process. The learning rate of the Gene step (i.e., *gene-lr*) controls the weight on genetic features during the training procedure, serving as a hyperparameter for different cases (**Result**). Other implementation details of the model, including network architectures, training details, algorithm, and training stopping criteria, are presented in **Supplementary eMethod 2**.

Subtype Assignment. After the training process, the clustering function g_1 can be applied to the training and independent test data to estimate the latent variable z_1 that indicates the subtypes of interest (i.e., categorical subgroup membership). Specifically, g_1 outputs M probability values (P_i) for each participant, with each probability corresponding to one subtype and the sum of M probabilities being 1 ($\sum_{i=1}^M P_i = 1$). We then assign each participant to the dominant subtype, determined by the maximum probability (subtype = $\arg \max_i P_i$).

Method 2. Study populations

MRI (**Method 3**) and clinical (**Method 4**) data used in this study were consolidated and harmonized by the Imaging-Based Coordinate System for Aging and Neurodegenerative Diseases (iSTAGING) study. The iSTAGING study comprises data acquired via various imaging protocols, scanners, data modalities, and pathologies, including more than 50,000 participants from more than 13 studies on 3 continents and encompassing a wide range of ages (22 to 90 years). Specifically, the current study used MRIs from the Alzheimer's Disease Neuroimaging Initiative (ADNI)⁶³, the UK Biobank (UKBB)⁶⁴, the Baltimore Longitudinal Study of Aging (BLSA)^{65,66}, the Australian Imaging, Biomarker, and Lifestyle study of aging (AIBL)⁶⁷, the Biomarkers of Cognitive Decline Among Normal Individuals in the Johns Hopkins (BIOCARD)⁶⁸, the Open Access Series of Imaging Studies (OASIS)⁶⁹, PENN, and the Wisconsin Registry for Alzheimer's Prevention (WRAP) studies⁷⁰. In addition, whole genome sequencing (WGS) data were collected for ADNI participants; the UKBB study also consolidated the imputed genotype data (**Method 5**). Demographics and the number of participants from each study are detailed in **Table 1**.

Study	N	Diagnosis				Age (years)	Sex (male/%)	Semi-synthetic	Real data experiments
		HC	MCI	AD	HTN				
ADNI	1533	472	784	277	0	73.58±7.15	848/55.3%	280	1533
UKBB	27,325	10,911	0	0	16,414	64.43±7.48	13,116/48.0%	0	27,325
BLSA	341	341	0	0	0	66.15±4.84	146/42.8%	341	0
AIBL	373	373	0	0	0	68.22±3.99	147/39.4%	373	0
BIOCARD	143	143	0	0	0	62.29±5.42	63/44.1%	143	0
OASIS	403	403	0	0	0	66.56±5.33	148/36.7%	403	0
PENN	107	107	0	0	0	67.18±4.30	31/29.0%	107	0
WRAP	90	90	0	0	0	63.60±5.21	27/30.0%	90	0

Table1. Participants and studies for the semi-synthetic and real data experiments. For age, the mean and the standard deviation are reported. For sex, the number of males and the percentage is presented. HTN: Hypertension; HC: healthy control; AD: clinical AD; MCI: mild cognitive impairment; Semi-synthetic: number of participants included in the semi-synthetic experiments; Real data experiments: number of participants included in the real data experiments.

Method 3. Image processing and harmonization

A fully automated pipeline was applied to process the T1-weighted MRIs. All MRIs were first corrected for intensity inhomogeneities.⁷¹ A multi-atlas skull stripping algorithm was applied to remove extra-cranial material.⁷² Subsequently, 144 anatomical ROIs were identified in gray matter (GM, 119 ROIs), white matter (WM, 19 ROIs), and ventricles (6 ROIs) using a multi-atlas label fusion method⁷³. Voxel-wise regional volumetric maps for GM and WM tissues (referred to as RAVENS)⁷⁴, were computed by spatially aligning skull-stripped images to a single subject brain template using a registration method⁷⁵. White matter hyperintensity (WMH) volumes were calculated through a deep-learning-based segmentation method⁷⁶ built upon the U-Net architecture⁷⁷, using inhomogeneity-corrected and co-registered FLAIR and T1-weighted images. Site-specific mean and variance were estimated with an extensively validated statistical harmonization method⁷⁸ in the healthy control population and applied to the entire population while controlling for covariates.

Method 4. Cognitive, clinical, CSF, and plasma biomarkers

For the real data experiments, we included CSF and plasma biomarkers, *APOE* $\epsilon 4$ alleles, and cognitive test scores provided by ADNI and UKBB. For ADNI, all measures were downloaded from the LONI website (<http://adni.loni.ucla.edu>). Detailed methods for CSF measurements of β -amyloid ($A\beta$) and phospho-tau (p-tau) are described in Hansson et al.⁷⁹ Other CSF and plasma biomarkers were measured using the multiplex xMAP Luminex platform, with details described in “Biomarkers Consortium ADNI Plasma Targeted Proteomics Project – Data Primer” (available at <http://adni.loni.ucla.edu>). The ADNI study has previously validated several composite cognitive scores across several domains, including ADNI-MEM⁸⁰, ADNI-EF⁸¹, and ADNI-LAN⁸². The UKBB study provides several cognitive tests, including DSST, TMT-A, and TMT-B, etc. (<https://biobank.ndph.ox.ac.uk/showcase/label.cgi?id=100026>).

Method 5. Genetic data processing and selection

Genetic analyses were performed using the whole-genome sequencing (WGS) data from ADNI and the imputed genotype data from UKBB. We performed a rigorous quality check procedure detailed in our previous papers⁶⁻⁸, which is also publicly available at our web portal: https://www.cbica.upenn.edu/bridgeport/data/pdf/BIGS_genetic_protocol.pdf.

To preselect disease-associated SNPs, we performed a manual search through the NHGRI-EBI GWAS Catalog⁸³. Specifically, we used the keywords “Alzheimer's disease biomarker measurement” for AD-associated SNPs and “hypertension” for hypertension-associated SNPs. We further filtered out SNPs with reported p-values greater than or equal to 5×10^{-8} , removed SNPs with MAF smaller than 5%, included studies from European ancestries, and removed SNPs in linkage disequilibrium (i.e., window size = 2000 kb, and $r^2 = 0.2$). Finally, we merged these preselected SNPs with our quality-checked WGS (AD) and imputed genotype data (hypertension). This procedure resulted in 1532 participants and 178 AD-associated SNPs for the MCI/clinical AD population and 33,541 participants and 117 hypertension-associated SNPs for the hypertension population.

Method 6. Semi-synthetic experiments

Data selection. For simulated imaging features, we imposed volume decrease in predefined imaging ROIs for a proportion of (1200 out of 1739) HC participants (i.e., Pseudo-PT participants), which we referred to as the semi-synthetic datasets. For simulated genetic features, we generated fully simulated SNP data for all Pseudo-PT participants. We included 1739 participants (age < 75 and MMSE > 28) from 7 different studies (**Table 1**) and defined 539 participants as the real HC group and the remaining 1200 participants as the Pseudo-PT group. The Pseudo-PT group was further divided into three ($M=3$) subgroups (three ground truth subtypes). Each subgroup was imposed with one specific imaging pattern and simulated genetic features – the ground truth for each subtype regarding imaging and genetic features.

Imaging feature construction. Three different imaging patterns were imposed on the Pseudo-PT participants within the three subgroups (**Figure 2e**). The volumes of selected ROIs were randomly decreased by 0-30%, being uniformly sampled within the range. In addition, we also introduced one or two imaging-specific confounding patterns ($n_{\text{confound}}=1$ or 2) (**Figure 2e**) to one or two sets of randomly sampled Pseudo-PT participants. Importantly, these Pseudo-PT participants possessed similar confounding patterns but did not share genetic features. Details of selected ROIs for the subtypes and the confounding patterns are presented in **Supplementary eData 6**.

Genetic feature construction. We constructed an n_{genetic} -dimensional vector for each Pseudo-PT indicating the counts of minor alleles (0, 1, or 2) of n_{genetic} SNPs. Each subtype was simulated to be associated with four SNPs (**Figure 2d**). That is, the MAF of each SNP within the subgroup was around 15% higher than the remaining participants – assuming the minor alleles are risk alleles for the simulated brain atrophy patterns. In addition, we constructed genetic-specific confounders by randomly sampling two other subgroups of Pseudo-PT and selecting four associated SNPs (i.e., confounding SNPs) for each subgroup (**Figure 2d**). Selected confounding SNPs could overlap with subtype-associated SNPs in the simulation. Other non-selected SNPs had a MAF of 33% in all Pseudo-PT participants. We set n_{genetic} to 100, 250, and 500 during the simulation. A higher n_{genetic} indicates more complex confounding factors and leads to a more difficult task for model validations.

Cross-validation. On the semi-synthetic datasets with the known ground truth, we performed fifty repetitions of stratified holdout cross-validation (CV, 80% of data for training, and 20% for testing) for two purposes. First, we set different values (i.e., 5×10^{-5} , 1×10^{-4} , 2×10^{-4} , 4×10^{-4}) for *gene-lr* (a hyperparameter introduced in **Method 1**) to test the generalizability of the models. Second, we used the CV procedure to select the optimal value of *gene-lr*. We proposed a new metric, *N-Asso-SNPs*, for hyperparameter selections in the semi-synthetic and real data experiments (**Method 8**), which indicates the SNP-subtype associations in the test set. We calculated a log-likelihood-ratio (llr) for each SNP, as introduced in **Method 8**. *N-Asso-SNPs* equals the number of SNPs with $llr > 3.841$. The optimal *gene-lr* was chosen based on the highest mean *N-Asso-SNPs*.

Missing SNP test. To test the influence of the missing SNPs in the genetic data, we randomly set 10%/20%/30% of the SNPs as missing values (NAN). We ran the Gene-SGAN model fifty times on each dataset with the optimal *gene-lr* selected through the abovementioned CV procedure.

Model comparisons. We compared Gene-SGAN with six previously proposed methods, including Smile-GAN, Deep Canonical Correlation Analysis (Deep-CCA), CCA, Multiview-spectral-clustering (MSC), Multiview-Kmeans (MKmeans), Kmeans. We ran the model fifty times on each dataset with different n_{genetic} and n_{confound} , and derived fifty clustering accuracies. Implementation details of the six previously proposed methods can be found in **Supplementary eMethod 3**.

The transformation function *f* for clinical interpretability. We used the trained function *f* to *post hoc* reveal imaging patterns related to each identified subtype. For the three inputs of *f*, we set z_1 to be the one-hot vector corresponding to the subtype; additionally, we sampled 539 x and z_2 from the HC population and the uniform distribution $U[0,1]^{n_{z_2}}$, respectively, without replacements. The mean value of 539 calculated change ratios, $\frac{1}{539} \sum_{x, z_2} (f(x, z_1, z_2) - x)/x$, indicates the imaging patterns that drive the solution of the searched subtypes. For example, we presented the average imaging patterns characterized by 50 models trained on the dataset with $n_{\text{genetic}}=100$ and $n_{\text{confound}}=2$ in **Figure 2e**.

The inference function *h* for clinical interpretability. The trained function *h* infers the genetic feature distribution corresponding to each subtype. For the two inputs of *h*, we set z_1 to be the corresponding one-hot vector and sampled 100 z_3 from $p(z_3) = N(0^{n_{z_3}}, 1^{n_{z_3}})$. The average of 100 outputs of *h*, $\frac{1}{100} \sum_{z_3} h(z_1, z_3)$, was considered the inferred MAFs of SNPs within each subtype. For example, we presented the average of MAFs inferred by 50 models trained on the dataset with $n_{\text{genetic}}=100$ and $n_{\text{confound}}=2$ in **Figure 2h**.

Method 7. Real data experiments

Data selection. For the study of MCI/AD, we included baseline participants of the ADNI study, comprised of 472 cognitively normal, 784 MCI, and 277 clinical AD participants. The 1061 MCI and clinical AD participants were defined as the patient group, and the remaining 472 cognitively normal participants were defined as the HC group. The 144 ROIs and the 178 AD-associated SNPs were used as phenotypic and genetic features, respectively. For the study of hypertension, we selected participants from the UKBB study. Participants were defined as hypertensive patients ($N=16,414$) if satisfying one of the three criteria: 1) systole > 130 and diastole > 80 ; 2) history of

hypertension (code 1065 or 1072 in UKBB data field: f.20002.0.0); 3) hypertension medication (UKBB data fields: f.6177.0.0 and f.6153.0.0). The HC group (N=10,911) was defined as the remaining participants with systole<130 and diastole<80. The 144 ROIs and WMH volume (available for all UKBB participants) were used as phenotypic features, and the 117 hypertension-associated SNPs were used as genetic features. In the split-sampled experiments for hypertension, we constructed one discovery set with 10,911 HC participants and 8207 hypertensive patients and one replication set with the remaining 8207 hypertensive patients.

Input features of Gene-SGAN. For both studies, The ROIs/WMH volumes of all participants were first residualized to rule out the covariate (i.e., age, sex, and ICV) effects estimated in the HC group via a linear regression model. Then, the adjusted features were standardized with respect to the HC group to ensure a mean of 1 and a standard deviation of 0.1 among the HC participants for each ROI. For the genetic features, each SNP allele was recoded into 0, 1, or 2, indicating the count of minor alleles per participant. The processed imaging and genetic features were used as inputs for the Gene-SGAN model.

Output subtypes of Gene-SGAN. For both studies of MCI/AD and hypertension, we derived three different resolutions of clustering solutions (M=3, 4, and 5). As introduced in **Method 6**, we selected *gene-lr* using fifty iterations of the CV procedure with *N-Asso-SNPs* as an evaluation metric. Specifically, the value of *gene-lr* (5×10^{-5} , 1×10^{-4} , 2×10^{-4} , 4×10^{-4}) leading to the highest mean *N-Asso-SNP* over all three resolutions (M) was considered optimal. Next, for each M, we utilized all fifty models to derive their consensus as the final participants' subtypes (i.e., ensemble learning). In the split-sampled experiments for the hypertension population, the fifty models trained using the discovery set were applied to the 8027 patients in the replication set for deriving their subtypes.

Method 8. Statistical analysis

To test differences in CSF/Plasma biomarkers among the M subtypes, we performed ANOVA tests and used the Benjamin-Hochberg method to correct for multiple comparisons. Pairwise subtype comparisons were performed for other clinical (e.g., cognitive scores) and demographic variables (e.g., age, sex). For continuous variables, we utilized Mann-Whitney U tests for certain variables due to large skewness (e.g., WMH), and student's t-tests otherwise. For categorical variables (e.g., sex), the chi-squared test was used.

To test SNP-subtype associations, we performed a likelihood-ratio test on multinomial logistic regression models with subtype memberships as dependent variables. Specifically, the log-likelihood-ratio (llr) was calculated between two models fitted with and without each SNP, adjusting for covariates, including age, sex, ICV, and the first five genetic principal components. For MCI/AD, the *APOE ε4* genotype was used as another covariate. The Bonferroni method was used to correct for multiple comparisons.

Data Availability

Data used for this study were provided from ADNI and UKBB studies via data sharing agreements that did not include permission to further share the data. Data from ADNI are available from the ADNI database (adni.loni.usc.edu) upon registration and compliance with the data usage agreement. Data from the UKBB are available upon request from the UKBB website (<https://www.ukbiobank.ac.uk/>). GWAS summary statistics are publicly available in supplementary data and at our BRIDGEPORT web portal: <https://www.cbica.upenn.edu/bridgeport/>.

Code Availability

The software and resources used in this study are all publicly available:

- Gene-SGAN: <https://pypi.org/project/GeneSGAN/>
- BRIDGEPORT: <https://www.cbica.upenn.edu/bridgeport/>
- MUSE: <https://www.med.upenn.edu/sbia/muse.html>

Authors' contributions

Mr. Yang has full access to all the data in the study and takes responsibility for the integrity of the data and the accuracy of the data analysis.

Study concept and design: Yang, Davatzikos

Acquisition, analysis, or interpretation of data: Yang, Davatzikos

Drafting of the manuscript: Yang, Wen, Davatzikos

Critical revision of the manuscript for important intellectual content: all authors

Statistical and genetic analysis: Yang

References

- 1 Davatzikos, C. Machine learning in neuroimaging: Progress and challenges. *Neuroimage* **197**, 652-656 (2019). <https://doi.org:10.1016/j.neuroimage.2018.10.003>
- 2 Davatzikos, C., Xu, F., An, Y., Fan, Y. & Resnick, S. M. Longitudinal progression of Alzheimer's-like patterns of atrophy in normal older adults: the SPARE-AD index. *Brain* **132**, 2026-2035 (2009). <https://doi.org:10.1093/brain/awp091>
- 3 Arbabshirani, M. R., Plis, S., Sui, J. & Calhoun, V. D. Single subject prediction of brain disorders in neuroimaging: Promises and pitfalls. *Neuroimage* **145**, 137-165 (2017). <https://doi.org:10.1016/j.neuroimage.2016.02.079>
- 4 Habes, M. *et al.* The Brain Chart of Aging: Machine-learning analytics reveals links between brain aging, white matter disease, amyloid burden, and cognition in the iSTAGING consortium of 10,216 harmonized MR scans. *Alzheimers Dement* **17**, 89-102 (2021). <https://doi.org:10.1002/alz.12178>
- 5 Elliott, L. T. *et al.* Genome-wide association studies of brain imaging phenotypes in UK Biobank. *Nature* **562**, 210-216 (2018). <https://doi.org:10.1038/s41586-018-0571-7>
- 6 Wen, J. *et al.* Novel genomic loci and pathways influence patterns of structural covariance in the human brain. *medRxiv*, 2022.2007.2020.22277727 (2022). <https://doi.org:10.1101/2022.07.20.22277727>
- 7 Wen, J. *et al.* Characterizing Heterogeneity in Neuroimaging, Cognition, Clinical Symptoms, and Genetics Among Patients With Late-Life Depression. *JAMA Psychiatry* **79**, 464-474 (2022). <https://doi.org:10.1001/jamapsychiatry.2022.0020>
- 8 Wen, J. *et al.* Genetic, clinical underpinnings of subtle early brain change along Alzheimer's dimensions. *bioRxiv*, 2022.2009.2016.508329 (2022). <https://doi.org:10.1101/2022.09.16.508329>
- 9 Vamathevan, J. *et al.* Applications of machine learning in drug discovery and development. *Nat Rev Drug Discov* **18**, 463-477 (2019). <https://doi.org:10.1038/s41573-019-0024-5>
- 10 O'Brien, J. T. *et al.* Vascular cognitive impairment. *Lancet Neurol* **2**, 89-98 (2003). [https://doi.org:10.1016/s1474-4422\(03\)00305-3](https://doi.org:10.1016/s1474-4422(03)00305-3)
- 11 Yang, Z. *et al.* A deep learning framework identifies dimensional representations of Alzheimer's Disease from brain structure. *Nature Communications* **12** (2021). <https://doi.org:10.1038/s41467-021-26703-z>
- 12 Young, A. L. *et al.* Uncovering the heterogeneity and temporal complexity of neurodegenerative diseases with Subtype and Stage Inference. *Nat Commun* **9**, 4273 (2018). <https://doi.org:10.1038/s41467-018-05892-0>
- 13 Zhang, X. *et al.* Bayesian model reveals latent atrophy factors with dissociable cognitive trajectories in Alzheimer's disease. *Proc Natl Acad Sci U S A* **113**, E6535-e6544 (2016). <https://doi.org:10.1073/pnas.1611073113>
- 14 Dong, A. *et al.* Heterogeneity of neuroanatomical patterns in prodromal Alzheimer's disease: links to cognition, progression and biomarkers. *Brain* **140**, 735-747 (2017). <https://doi.org:10.1093/brain/aww319>
- 15 Varol, E., Sotiras, A., Davatzikos, C. & Alzheimer's Disease Neuroimaging, I. HYDRA: Revealing heterogeneity of imaging and genetic patterns through a multiple max-margin discriminative analysis framework. *Neuroimage* **145**, 346-364 (2017). <https://doi.org:10.1016/j.neuroimage.2016.02.041>
- 16 Kendler, K. S. & Neale, M. C. Endophenotype: a conceptual analysis. *Mol Psychiatry* **15**, 789-797 (2010). <https://doi.org:10.1038/mp.2010.8>

- 17 Goodfellow, I. *et al.* Generative Adversarial Networks. *Advances in Neural Information Processing Systems* **3** (2014). <https://doi.org:10.1145/3422622>
- 18 Esiri, M. M., Nagy, Z., Smith, M. Z., Barnetson, L. & Smith, A. D. Cerebrovascular disease and threshold for dementia in the early stages of Alzheimer's disease. *Lancet* **354**, 919-920 (1999). [https://doi.org:10.1016/s0140-6736\(99\)02355-7](https://doi.org:10.1016/s0140-6736(99)02355-7)
- 19 Hotelling, H. Relations Between Two Sets of Variables. *Biometrika* **28**, 321-377 (1936). <https://doi.org:10.1093/biomet/28.3-4.321>
- 20 Andrew, G., Arora, R., Bilmes, J. & Livescu, K. Deep Canonical Correlation Analysis. *Proceedings of the 30th International Conference on Machine Learning*, 1247-1255 (2013).
- 21 Kumar, A. & Daumé, H. A Co-training Approach for Multi-view Spectral Clustering. *Proceedings of the 28th International Conference on International Conference on Machine Learning*, 393-400 (2011).
- 22 Bickel, S. & Scheffer, T. Multi-view clustering. *Fourth IEEE International Conference on Data Mining (ICDM'04)*, 19-26 (2004).
- 23 Lloyd, S. Least squares quantization in PCM. *IEEE Transactions on Information Theory* **28**, 129-137 (1982). <https://doi.org:10.1109/TIT.1982.1056489>
- 24 Liu, C. C., Liu, C. C., Kanekiyo, T., Xu, H. & Bu, G. Apolipoprotein E and Alzheimer disease: risk, mechanisms and therapy. *Nat Rev Neurol* **9**, 106-118 (2013). <https://doi.org:10.1038/nrneurol.2012.263>
- 25 Fisher, M. J. Brain regulation of thrombosis and hemostasis: from theory to practice. *Stroke* **44**, 3275-3285 (2013). <https://doi.org:10.1161/strokeaha.113.000736>
- 26 Suidan, G. L. *et al.* Endothelial Von Willebrand factor promotes blood-brain barrier flexibility and provides protection from hypoxia and seizures in mice. *Arterioscler Thromb Vasc Biol* **33**, 2112-2120 (2013). <https://doi.org:10.1161/atvbaha.113.301362>
- 27 Pons, V. & Rivest, S. New Therapeutic Avenues of mCSF for Brain Diseases and Injuries. *Front Cell Neurosci* **12**, 499 (2018). <https://doi.org:10.3389/fncel.2018.00499>
- 28 Tan, J. *et al.* CD40 is expressed and functional on neuronal cells. *Embo j* **21**, 643-652 (2002). <https://doi.org:10.1093/emboj/21.4.643>
- 29 Ciesielski-Treska, J. *et al.* Chromogranin A induces a neurotoxic phenotype in brain microglial cells. *J Biol Chem* **273**, 14339-14346 (1998). <https://doi.org:10.1074/jbc.273.23.14339>
- 30 Dutta, G., Barber, D. S., Zhang, P., Doperalski, N. J. & Liu, B. Involvement of dopaminergic neuronal cystatin C in neuronal injury-induced microglial activation and neurotoxicity. *J Neurochem* **122**, 752-763 (2012). <https://doi.org:10.1111/j.1471-4159.2012.07826.x>
- 31 Ponomarev, E. D., Shriver, L. P. & Dittel, B. N. CD40 expression by microglial cells is required for their completion of a two-step activation process during central nervous system autoimmune inflammation. *J Immunol* **176**, 1402-1410 (2006). <https://doi.org:10.4049/jimmunol.176.3.1402>
- 32 Jochemsen, H. M. *et al.* The association of angiotensin-converting enzyme with biomarkers for Alzheimer's disease. *Alzheimers Res Ther* **6**, 27 (2014). <https://doi.org:10.1186/alzrt257>
- 33 Ashok, A., Rai, N. K., Raza, W., Pandey, R. & Bandyopadhyay, S. Chronic cerebral hypoperfusion-induced impairment of A β clearance requires HB-EGF-dependent sequential activation of HIF1 α and MMP9. *Neurobiol Dis* **95**, 179-193 (2016). <https://doi.org:10.1016/j.nbd.2016.07.013>

- 34 Leng, F. & Edison, P. Neuroinflammation and microglial activation in Alzheimer disease: where do we go from here? *Nat Rev Neurol* **17**, 157-172 (2021). <https://doi.org:10.1038/s41582-020-00435-y>
- 35 Selkoe, D. J. & Hardy, J. The amyloid hypothesis of Alzheimer's disease at 25 years. *EMBO Mol Med* **8**, 595-608 (2016). <https://doi.org:10.15252/emmm.201606210>
- 36 Sweeney, M. D., Sagare, A. P. & Zlokovic, B. V. Blood-brain barrier breakdown in Alzheimer disease and other neurodegenerative disorders. *Nat Rev Neurol* **14**, 133-150 (2018). <https://doi.org:10.1038/nrneurol.2017.188>
- 37 Sargurupremraj, M. *et al.* Cerebral small vessel disease genomics and its implications across the lifespan. *Nat Commun* **11**, 6285 (2020). <https://doi.org:10.1038/s41467-020-19111-2>
- 38 Mendez, M. F. Early-onset Alzheimer Disease and Its Variants. *Continuum (Minneapolis Minn)* **25**, 34-51 (2019). <https://doi.org:10.1212/con.0000000000000687>
- 39 Fleisher, A. *et al.* Sex, apolipoprotein E epsilon 4 status, and hippocampal volume in mild cognitive impairment. *Arch Neurol* **62**, 953-957 (2005). <https://doi.org:10.1001/archneur.62.6.953>
- 40 Deary, I. J. *et al.* Cognitive change and the APOE epsilon 4 allele. *Nature* **418**, 932 (2002). <https://doi.org:10.1038/418932a>
- 41 Jansen, I. E. *et al.* Genome-wide meta-analysis identifies new loci and functional pathways influencing Alzheimer's disease risk. *Nat Genet* **51**, 404-413 (2019). <https://doi.org:10.1038/s41588-018-0311-9>
- 42 Lambert, J. C. *et al.* Meta-analysis of 74,046 individuals identifies 11 new susceptibility loci for Alzheimer's disease. *Nat Genet* **45**, 1452-1458 (2013). <https://doi.org:10.1038/ng.2802>
- 43 Sawcer, S. *et al.* Genetic risk and a primary role for cell-mediated immune mechanisms in multiple sclerosis. *Nature* **476**, 214-219 (2011). <https://doi.org:10.1038/nature10251>
- 44 Murray, M. E. *et al.* Neuropathologically defined subtypes of Alzheimer's disease with distinct clinical characteristics: a retrospective study. *Lancet Neurol* **10**, 785-796 (2011). [https://doi.org:10.1016/S1474-4422\(11\)70156-9](https://doi.org:10.1016/S1474-4422(11)70156-9)
- 45 Jun, G. R. *et al.* Transethnic genome-wide scan identifies novel Alzheimer's disease loci. *Alzheimers Dement* **13**, 727-738 (2017). <https://doi.org:10.1016/j.jalz.2016.12.012>
- 46 Jenkins, L. M. *et al.* Cumulative Blood Pressure Exposure, Basal Ganglia, and Thalamic Morphology in Midlife. *Hypertension* **75**, 1289-1295 (2020). <https://doi.org:10.1161/hypertensionaha.120.14678>
- 47 Maillard, P. *et al.* Effects of systolic blood pressure on white-matter integrity in young adults in the Framingham Heart Study: a cross-sectional study. *Lancet Neurol* **11**, 1039-1047 (2012). [https://doi.org:10.1016/s1474-4422\(12\)70241-7](https://doi.org:10.1016/s1474-4422(12)70241-7)
- 48 McEvoy, L. K. *et al.* Hypertension-related alterations in white matter microstructure detectable in middle age. *Hypertension* **66**, 317-323 (2015). <https://doi.org:10.1161/hypertensionaha.115.05336>
- 49 Roberts, R. O. *et al.* Association of type 2 diabetes with brain atrophy and cognitive impairment. *Neurology* **82**, 1132-1141 (2014). <https://doi.org:10.1212/wnl.0000000000000269>
- 50 Moran, C. *et al.* Brain atrophy in type 2 diabetes: regional distribution and influence on cognition. *Diabetes Care* **36**, 4036-4042 (2013). <https://doi.org:10.2337/dc13-0143>

- 51 Beauchet, O. *et al.* Blood pressure levels and brain volume reduction: a systematic review and meta-analysis. *J Hypertens* **31**, 1502-1516 (2013). <https://doi.org/10.1097/HJH.0b013e32836184b5>
- 52 de Leeuw, F. E. *et al.* Hypertension and cerebral white matter lesions in a prospective cohort study. *Brain* **125**, 765-772 (2002). <https://doi.org/Doi.10.1093/Brain/Awf077>
- 53 Chand, G. B. *et al.* Two distinct neuroanatomical subtypes of schizophrenia revealed using machine learning. *Brain* **143**, 1027-1038 (2020). <https://doi.org/10.1093/brain/awaa025>
- 54 Morris, A. P. *et al.* Large-scale association analysis provides insights into the genetic architecture and pathophysiology of type 2 diabetes. *Nat Genet* **44**, 981-990 (2012). <https://doi.org/10.1038/ng.2383>
- 55 Sakaue, S. *et al.* A cross-population atlas of genetic associations for 220 human phenotypes. *Nat Genet* **53**, 1415-1424 (2021). <https://doi.org/10.1038/s41588-021-00931-x>
- 56 Vujkovic, M. *et al.* Discovery of 318 new risk loci for type 2 diabetes and related vascular outcomes among 1.4 million participants in a multi-ancestry meta-analysis. *Nat Genet* **52**, 680-691 (2020). <https://doi.org/10.1038/s41588-020-0637-y>
- 57 Turcot, V. *et al.* Protein-altering variants associated with body mass index implicate pathways that control energy intake and expenditure in obesity. *Nat Genet* **50**, 26-41 (2018). <https://doi.org/10.1038/s41588-017-0011-x>
- 58 Gibney, E. Could machine learning fuel a reproducibility crisis in science? *Nature* **608**, 250-251 (2022). <https://doi.org/10.1038/d41586-022-02035-w>
- 59 Kraft, P., Zeggini, E. & Ioannidis, J. P. Replication in genome-wide association studies. *Stat Sci* **24**, 561-573 (2009). <https://doi.org/10.1214/09-sts290>
- 60 Finan, C. *et al.* The druggable genome and support for target identification and validation in drug development. *Sci Transl Med* **9** (2017). <https://doi.org/10.1126/scitranslmed.aag1166>
- 61 Wen, J. *et al.* Subtyping brain diseases from imaging data. *ArXiv* (2022).
- 62 Mattei, P.-A. & Frellsen, J. in *Proceedings of the 36th International Conference on Machine Learning* Vol. 97 (eds Chaudhuri Kamalika & Salakhutdinov Ruslan) 4413--4423 (PMLR, Proceedings of Machine Learning Research, 2019).
- 63 Petersen, R. C. *et al.* Alzheimer's Disease Neuroimaging Initiative (ADNI): clinical characterization. *Neurology* **74**, 201-209 (2010). <https://doi.org/10.1212/WNL.0b013e3181cb3e25>
- 64 Miller, K. L. *et al.* Multimodal population brain imaging in the UK Biobank prospective epidemiological study. *Nat Neurosci* **19**, 1523-1536 (2016). <https://doi.org/10.1038/nn.4393>
- 65 Resnick, S. M. *et al.* One-year age changes in MRI brain volumes in older adults. *Cerebral Cortex* **10**, 464-472 (2000).
- 66 Resnick, S. M., Pham, D. L., Kraut, M. A., Zonderman, A. B. & Davatzikos, C. Longitudinal Magnetic Resonance Imaging Studies of Older Adults: A Shrinking Brain. *The Journal of Neuroscience* **23**, 295-301 (2003).
- 67 Ellis, K. A. *et al.* The Australian Imaging, Biomarkers and Lifestyle (AIBL) study of aging: methodology and baseline characteristics of 1112 individuals recruited for a longitudinal study of Alzheimer's disease. *Int Psychogeriatr* **21**, 672-687 (2009). <https://doi.org/10.1017/s1041610209009405>

- 68 Soldan, A. *et al.* Relationship of medial temporal lobe atrophy, APOE genotype, and cognitive reserve in preclinical Alzheimer's disease. *Hum Brain Mapp* **36**, 2826-2841 (2015). <https://doi.org:10.1002/hbm.22810>
- 69 LaMontagne, P. J. *et al.* OASIS-3: Longitudinal Neuroimaging, Clinical, and Cognitive Dataset for Normal Aging and Alzheimer Disease. *medRxiv*, 2019.2012.2013.19014902 (2019). <https://doi.org:10.1101/2019.12.13.19014902>
- 70 Johnson, S. C. *et al.* The Wisconsin Registry for Alzheimer's Prevention: A review of findings and current directions. *Alzheimers Dement (Amst)* **10**, 130-142 (2018). <https://doi.org:10.1016/j.dadm.2017.11.007>
- 71 Sled, J. G., Zijdenbos, A. P. & Evans, A. C. A nonparametric method for automatic correction of intensity nonuniformity in MRI data. *IEEE Trans Med Imaging* **17**, 87-97 (1998). <https://doi.org:10.1109/42.668698>
- 72 Doshi, J., Erus, G., Ou, Y., Gaonkar, B. & Davatzikos, C. Multi-atlas skull-stripping. *Acad Radiol* **20**, 1566-1576 (2013). <https://doi.org:10.1016/j.acra.2013.09.010>
- 73 Doshi, J. *et al.* MUSE: MUlTI-atlas region Segmentation utilizing Ensembles of registration algorithms and parameters, and locally optimal atlas selection. *NeuroImage* **127**, 186-195 (2016). <https://doi.org:10.1016/j.neuroimage.2015.11.073>
- 74 Davatzikos, C., Genc, A., Xu, D. & Resnick, S. M. Voxel-based morphometry using the RAVENS maps: methods and validation using simulated longitudinal atrophy. *Neuroimage* **14**, 1361-1369 (2001). <https://doi.org:10.1006/nimg.2001.0937>
- S1053-8119(01)90937-1 [pii]
- 75 Ou, Y., Sotiras, A., Paragios, N. & Davatzikos, C. DRAMMS: Deformable registration via attribute matching and mutual-saliency weighting. *Med Image Anal* **15**, 622-639 (2011). [https://doi.org:S1361-8415\(10\)00094-0](https://doi.org:S1361-8415(10)00094-0) [pii]
- 10.1016/j.media.2010.07.002
- 76 Doshi, J. *et al.* MUSE: MUlTI-atlas region Segmentation utilizing Ensembles of registration algorithms and parameters, and locally optimal atlas selection. *Neuroimage* **127**, 186-195 (2016). <https://doi.org:10.1016/j.neuroimage.2015.11.073>
- 77 Ronneberger, O., Fischer, P., Brox, T. (ed ArXiv e-prints) (2015).
- 78 Pomponio, R. *et al.* Harmonization of large MRI datasets for the analysis of brain imaging patterns throughout the lifespan. *Neuroimage* **208**, 116450 (2020). <https://doi.org:10.1016/j.neuroimage.2019.116450>
- 79 Hansson, O. *et al.* CSF biomarkers of Alzheimer's disease concord with amyloid- β PET and predict clinical progression: A study of fully automated immunoassays in BioFINDER and ADNI cohorts. *Alzheimers Dement* **14**, 1470-1481 (2018). <https://doi.org:10.1016/j.jalz.2018.01.010>
- 80 Crane, P. K. *et al.* Development and assessment of a composite score for memory in the Alzheimer's Disease Neuroimaging Initiative (ADNI). *Brain Imaging Behav* **6**, 502-516 (2012). <https://doi.org:10.1007/s11682-012-9186-z>
- 81 Gibbons, L. E. *et al.* A composite score for executive functioning, validated in Alzheimer's Disease Neuroimaging Initiative (ADNI) participants with baseline mild cognitive impairment. *Brain Imaging Behav* **6**, 517-527 (2012). <https://doi.org:10.1007/s11682-012-9176-1>
- 82 Choi, S. E. *et al.* Development and validation of language and visuospatial composite scores in ADNI. *Alzheimers Dement (N Y)* **6**, e12072 (2020). <https://doi.org:10.1002/trc2.12072>

83 Buniello, A. *et al.* The NHGRI-EBI GWAS Catalog of published genome-wide association studies, targeted arrays and summary statistics 2019. *Nucleic Acids Res* **47**, D1005-d1012 (2019). <https://doi.org:10.1093/nar/gky1120>

Acknowledgments

The iSTAGING consortium is a multi-institutional effort funded by NIA by RF1 AG054409. The Baltimore Longitudinal Study of Aging neuroimaging study is funded by the Intramural Research Program, National Institute on Aging, National Institutes of Health and by HHSN271201600059C. Other supporting grants include 5U01AG068057-02, 1U24AG074855-01. S.R.H and J.C.M are supported by multiple grants and contracts from NIH. A.A. was supported by grants 191026 and 206795 from the Swiss National Science Foundation. This research has been conducted using the UK Biobank Resource under Application Number 35148. Data used in the preparation of this article were in part obtained from the Alzheimer's Disease Neuroimaging Initiative (ADNI) database (adni.loni.usc.edu). As such, the investigators within the ADNI contributed to the design and implementation of ADNI and/or provided data but did not participate in the analysis or writing of this report. A complete listing of ADNI investigators can be found at: http://adni.loni.usc.edu/wpcontent/uploads/how_to_apply/ADNI_Acknowledgement_List.pdf. ADNI is funded by the National Institute on Aging, the National Institute of Biomedical Imaging and Bioengineering, and through generous contributions from the following: AbbVie, Alzheimer's Association; Alzheimer's Drug Discovery Foundation; Araclon Biotech; BioClinica, Inc.; Biogen; Bristol-Myers Squibb Company; CereSpir, Inc.; Cogstate; Eisai Inc.; Elan Pharmaceuticals, Inc.; Eli Lilly and Company; EuroImmun; F. Hoffmann-La Roche Ltd and its affiliated company Genentech, Inc.; Fujirebio; GE Healthcare; IXICO Ltd.; Janssen Alzheimer Immunotherapy Research & Development, LLC.; Johnson & Johnson Pharmaceutical Research & Development LLC.; Lumosity; Lundbeck; Merck & Co., Inc.; Meso Scale Diagnostics, LLC.; NeuroRx Research; Neurotrack Technologies; Novartis Pharmaceuticals Corporation; Pfizer Inc.; Piramal Imaging; Servier; Takeda Pharmaceutical Company; and Transition Therapeutics. The Canadian Institutes of Health Research is providing funds to support ADNI clinical sites in Canada. Private sector contributions are facilitated by the Foundation for the National Institutes of Health (www.fnih.org). The grantee organization is the Northern California Institute for Research and Education, and the study is coordinated by the Alzheimer's Therapeutic Research Institute at the University of Southern California. ADNI data are disseminated by the Laboratory for Neuro Imaging at the University of Southern California. Mr. Yang had full access to all the data in the study. He took responsibility for the integrity of the data and the accuracy of the data analysis.

Gene-SGAN: a method for discovering disease subtypes with imaging and genetic signatures via multi-view weakly-supervised deep clustering

Supplementary Information

eMethod 1: Gene-SGAN: supplementary methodological details.

eMethod 1.1: Application of the inverse function for the subtype derivations.

eMethod 1.2: Modification of the GAN loss in the Gene-SGAN model: Motivation and Derivation.

eMethod 1.3: Derivation of the ELBO for the Gene Step.

eMethod 2: Implementation details of the Gene-SGAN model.

eMethod 2.1 Model Architectures.

eMethod 2.2 Training Details.

eMethod 3: Implementation details of model comparisons in the semi-synthetic experiments.

eMethod 4: Replication analyses for SNP-subtype associations.

eMethod 5: Examination of genetic and phenotypic variations captured by z_2 and z_3 .

eMethod 5.1 Associations of z_2 and z_3 with imaging volumetric measures.

eMethod 5.2 Associations of z_2 and z_3 with AD-associated SNPs.

eTable 1: Network architectures of the function f .

eTable 2: Network architectures of the functions D , g_1 & g_2 , h , r .

eTable 3: Implementation details of six compared methods.

eAlgorithm 1: Gene-SGAN training procedure.

eFigure 1: Gene-SGAN shows robust generalizability to test data in cross validation experiments on semi-synthetic datasets

eFigure 2: Gene-SGAN provides consistent and refined multiscale imaging subtypes related to AD.

eFigure 3: Gene-SGAN provides consistent and refined multiscale imaging subtypes related to hypertension.

eFigure 4. z_2 and z_3 variables capture additional non-linked imaging-specific and genetic-specific variations among MCI/AD participants.

eData 1: Associations between SNP variants and subtypes related to AD.

eData 2: CSF/Plasma biomarkers that are significantly different among four AD-related subtypes.

eData 3: Associations between SNP variants and subtypes related to hypertension.

eData 4: Replicated SNP-subtype associations in the split-sampled experiment.

eData 5: Associations between SNP variants and SmileGAN subtypes

eData 6: ROIs included in the simulated imaging patterns for the semi-synthetic experiments.

eMethod 1: Gene-SGAN: supplementary methodological details

eMethod 1.1: Application of the inverse functions for the subtype derivations.

The clustering function, g_1 , is applied to the training and independent test data to derive their subtypes of interest. As introduced in **Method 1**, through GAN and regularization, we encourage that the transformation function approximates the underlying pathological process h . After the training process, we assume that $p_{\text{syn}}(f(x, z_1, z_2)) \approx p_{\text{tar}}(y)$ and that the function f satisfies the constraints imposed by regularization. Thus, we consider the learned transformation function f a good approximation of the underlying function h , such that $f(x, z_1, z_2) \approx h(x, \sigma_1(z_1), \sigma_2(z_2))$, where $\sigma_i \in \Omega_i$ and Ω_i is a class of permutation functions that change the order of elements in the latent variables z_1 and z_2 . Since the orders of elements in the latent variables are unimportant and we can always change the orders of the derived subtypes, we rewrite the equation as $f(x, z_1, z_2) \approx h(x, z_1, z_2)$ without loss of generality. For any real patient data, $\bar{y} = h(\bar{x}, \bar{z}_1, \bar{z}_2) \sim p_{\text{tar}}(y)$, we can estimate its ground truth subtype, represented by \bar{z}_1 , through $g_1(\bar{y}) = g_1(h(\bar{x}, \bar{z}_1, \bar{z}_2)) \approx g_1(f(\bar{x}, \bar{z}_1, \bar{z}_2)) \approx \bar{z}_1$.

eMethod 1.2: Modification of the GAN loss in the Gene-SGAN model: Motivation and Derivation.

In most GAN-based models^{1,2}, including Smile-GAN³, the latent variables or noise variables are sampled from fixed distributions (e.g., gaussian or uniform distribution) predefined before the training process. The fixed latent distributions mostly do not affect the models' performances in generating realistic data. However, they are problematic if we use an inverse function to re-estimate the latent variables of the data. We focus on modifying the distribution of the major latent variable z_1 since we mainly focus on using the inverse function g_1 to re-estimate z_1 , which defines the subtypes of interests.

As introduced in **Supplementary eMethod 1.1**, we assume the inverse consistency, $g_1(f(x, z_1, z_2)) \approx z_1$, and equality in distributions, $p_{\text{syn}}(f(x, z_1, z_2)) \approx p_{\text{tar}}(y)$, after the training process. We can further derive that $p(g_1(y)) \approx p(g_1(f(x, z_1, z_2))) \approx p(z_1)$, where $p(g_1(y))$ is the distribution of patients' subtype memberships. Therefore, if we sample z_1 from a uniform categorical distribution, the sizes of derived subtype memberships will also be balanced, which leads to bias when the ground-truth subtypes are not uniformly distributed.

In real applications, we can never acquire the exact equality of distributions, $p(f(x, z_1, z_2)) = p_{\text{tar}}(y)$. Thus, a slight deviation of the ground truth latent distribution from the uniform distribution does not significantly affect the models' performances. However, a severe imbalance in the sizes of ground truth subtypes does affect the Smile-GAN³ and Gene-SGAN models if we sample the latent variable from the uniform distribution.

To resolve this issue, we make changes to the GAN loss function so that z_1 is implicitly sampled from a parametrized distribution, $p_{\theta_{z_1}}(z_1)$, which is optimized to approximate the ground truth latent distribution. With e_i defined as a one-hot vector with one at the i_{th} dimension, we derive that:

$$\begin{aligned} L_{\text{GAN}}(\theta_D, \theta_f, \theta_{z_1}) &= E_{y \sim p_{\text{tar}}(y)} [\log(D(y))] + E_{y' \sim p_{\text{syn}}(y')} [1 - \log(D(y'))] \quad (1) \\ &= E_{z_1 \sim p_{\theta_{z_1}}(z_1), y \sim p_{\text{tar}}(y)} [\log(D(y))] \end{aligned}$$

$$+ E_{z_1 \sim p_{\theta_{z_1}}(z_1), z_2 \sim p_{z_2}(z_2), x \sim p_{\text{ref}}(x)} [1 - \log(D(f(x, z_1, z_2)))] \quad (2)$$

$$= \sum_{i=1}^M p_{\theta_{z_1}}(e_i) E_{y \sim p_{\text{tar}}(y)} [\log(D(y))] \\ + \sum_{i=1}^M p_{\theta_{z_1}}(e_i) E_{z_2 \sim p_{z_2}(z_2), x \sim p_{\text{ref}}(x)} \left[1 - \log \left(D(f(x, e_i, z_2)) \right) \right] \quad (3)$$

$$= M * \sum_{i=1}^M p_U(e_i) p_{\theta_{z_1}}(e_i) E_{y \sim p_{\text{tar}}(y)} [\log(D(y))] \\ + M * \sum_{i=1}^M p_U(e_i) p_{\theta_{z_1}}(e_i) E_{z_2 \sim p_{z_2}(z_2), x \sim p_{\text{ref}}(x)} \left[1 - \log \left(D(f(x, e_i, z_2)) \right) \right] \quad (4)$$

$$= M * E_{y \sim p_{\text{tar}}(y), z_1 \sim p_U(z_1)} \left[p_{\theta_{z_1}}(z_1) \log(D(y)) \right] \\ + M * E_{z_1 \sim p_U(z_1), z_2 \sim p_{z_2}(z_2), x \sim p_{\text{ref}}(x)} \left[p_{\theta_{z_1}}(z_1) \left(1 - \log \left(D(f(x, z_1, z_2)) \right) \right) \right] \quad (5)$$

We derive the updated GAN loss function (5) from the basic objective function (1) presented in Goodfellow et al¹. The updated loss function enables us to sample z_1 from a uniform distribution but penalizes the losses with their probability under the distribution $p_{\theta_{z_1}}(z_1)$. In the training procedure, we only sample one value of z_1 for each x per batch instead of taking the expectation over all M categories. Therefore, to penalize both terms equally, the same modification is also applied to the first term of the equation (5), in which z_1 was not originally included.

Additionally, to prevent $p_{\theta_{z_1}}$ from converging to an extreme distribution (e.g., the probability of one category converges to zero), we added a regularization term that controls the distance between $p_{\theta_{z_1}}(z_1)$ and $p_U(z_1)$. Therefore, the final modified GAN loss function equals:

$$L_{\text{GAN}}(\theta_D, \theta_f, \theta_{z_2}) = M * E_{y \sim p_{\text{tar}}(y), z_1 \sim p_U(z_1)} \left[p_{\theta_{z_1}}(z_1) \log(D(y)) \right] \\ + M * E_{z_1 \sim p_U(z_1), z_2 \sim p_{z_2}(z_2), x \sim p_{\text{ref}}(x)} \left[p_{\theta_{z_1}}(z_1) \left(1 - \log \left(D(f(x, z_1, z_2)) \right) \right) \right] \\ + \kappa D_{\text{KL}}(p_U(z_1) | p_{\theta_{z_1}}(z_1))$$

eMethod 1.3: Derivation of the ELBO for the Gene Step.

In the Gene step, we attempted to approximate the intractable posterior distribution, $p_{\theta_h, \theta_{g_1}}(z_3 | v, y)$, by the variational distribution $q_{\theta_r}(z_3 | v, y)$. The KL divergence between $p_{\theta_h, \theta_{g_1}}(z_3 | v, y)$, and $q_{\theta_r}(z_3 | v, y)$ equals:

$$D_{\text{KL}} \left(q_{\theta_r}(z_3 | v, y) \middle| p_{\theta_h, \theta_{g_1}}(z_3 | v, y) \right) = E_{z_3 \sim q_{\theta_r}(z_3 | v, y)} [\log q_{\theta_r}(z_3 | v, y) - \log p_{\theta_h, \theta_{g_1}}(z_3 | v, y)] \\ = E_{z_3 \sim q_{\theta_r}(z_3 | v, y)} \left[\log q_{\theta_r}(z_3 | v, y) - \log \frac{p_{\theta_h, \theta_{g_1}}(z_3, v, y)}{p(v, y)} \right]$$

Since the latent variable z_3 characterizes genetic-specific variations, it is independent of y , and the KL divergence can be further written as:

$$D_{\text{KL}} \left(q_{\theta_r}(z_3 | v, y) \middle| p_{\theta_h, \theta_{g_1}}(z_3 | v, y) \right) \\ = E_{z_3 \sim q_{\theta_r}(z_3 | v, y)} \left[\log q_{\theta_r}(z_3 | v, y) - \log \frac{p_{\theta_h, \theta_{g_1}}(v | z_3, y) p_{z_3}(z_3) p(y)}{p(v | y) p(y)} \right] \\ = E_{z_3 \sim q_{\theta_r}(z_3 | v, y)} \left[\log q_{\theta_r}(z_3 | v, y) - \log p_{\theta_h, \theta_{g_1}}(v | z_3, y) - \log p_{z_3}(z_3) + \log p(v | y) \right]$$

From this equation, we can further derive the ELBO for $p(v | y)$:

$$\log p(v|y) \geq E_{z_3 \sim q_{\theta_r}(z_3|v, y)} [\log p_{\theta_h, \theta_{g_1}}(v|z_3, y) + \log \frac{p_{z_3}(z_3)}{q_{\theta_r}(z_3|v, y)}]$$

eMethod 2: Implementation details of Gene-SGAN

eMethod 2.1 Model Architectures

The general architectures of the neural networks can be understood from **Figure 1b**. In the semi-synthetic and real data experiments, the dimensions of z_2 and z_3 are both set to five (i.e., $n_{z_2} = n_{z_3} = 5$); the dimension of the phenotypic features equals 144 or 145 in different cases. In the Phenotype step, the transformation function f utilizes an encoding-decoding structure. The REF features x and the concatenation of z_1 and z_2 are first mapped to two vectors with the dimension of 36, respectively. Their element-wise multiplication is then decoded to construct the synthesized TAR features y' with dimensions 144 or 145. The inverse mapping functions g_1 and g_2 share the same network, which maps the real/synthesized TAR features y/y' to a vector with dimension $(5+M)$. The last five elements represent the re-estimated z_2 , while a Softmax function is applied to the first M elements to derive M probability values. The discriminator D utilizes an encoding structure that maps the real/synthesized TAR features y/y' to a vector with dimension two. In the Gene step, the concatenation of z_3 and $g_1(y)$ is mapped to an n_{genetic} -dimensional vector through a decoding neural network (i.e., the function h), which outputs the MAF of each SNP. The function r is backboneed by an encoding neural network that maps the concatenated genetic and imaging data to a vector with dimension ten. More details of model architectures can be found in **eTable 1** and **eTable 2**.

eMethod 2.2 Training Details

We set $\mu = 5$, $\lambda = 9$, and $\kappa = 0.1$ for all semi-synthetic and real data experiments. During the optimization procedure, the Phenotype and Gene steps were performed iteratively. Within the Phenotype step, we iteratively updated the parameters of the Discriminator (θ_D), the latent distribution (θ_{z_1}), as well as the transformation and reconstruction functions (θ_f , θ_{g_1} , and θ_{g_2}). The detailed training procedure is revealed by **eAlgorithm 1**. The ADAM optimizer⁴ was used with a learning rate (lr) 2×10^{-4} for θ_D , 2.5×10^{-5} for θ_{z_1} , and 1×10^{-3} for θ_f , θ_{g_1} , and θ_{g_2} . The learning rate of the Gene step (referred to as *gene-lr*) is a hyperparameter to be selected, as discussed in **Result** and **Method 6**. β_1 and β_2 for ADAM were set to be 0.5 and 0.999, respectively. Also, we performed gradient clipping for each iteration to avoid gradient explosions during the training process. The model was trained for at least 20000 iterations and saved until the Wasserstein Distance was smaller than 0.12 and the Alteration Quantity was smaller than 1/40 of the patients' sample sizes³.

We performed weight clipping⁵ to ensure the Lipschitz continuity of the transformation function and inverse functions. With Θ_f , Θ_{g_1} , and Θ_{g_2} denoting the weight spaces of f , g_1 , and g_2 , their compactness implies the Lipschitz continuity of the three functions. The compactness of Θ_f , Θ_{g_1} , and Θ_{g_2} was guaranteed by clapping these weight spaces into three closed boxes, $\Theta_f = [-c_f, c_f]^d$, $\Theta_{g_1} = [-c_{g_1}, c_{g_1}]^d$, and $\Theta_{g_2} = [-c_{g_2}, c_{g_2}]^d$. In the implementations, all clapping bounds were set to be 0.5 but can be further relaxed.

eTable 1: Network architectures of the function f

	Layer	Input Size	Bias Term	Leaky Relu α	Output Size
Encoder from x	Linear1+Leaky-Relu	144 or 145	No	0.2	72
	Linear2+Leaky-Relu	72	No	0.2	36
Decoder from z_1, z_2	Linear1+Sigmoid	5+M	Yes	NA	36
Decoder to y'	Linear1+Leaky-Relu	36	No	0.2	72
	Linear2+Leaky-Relu	72	No	0.2	144 or 145
	Linear3	144 or 145	No	NA	144 or 145

eTable 2: Network architecture of the functions D, g_1 & g_2 , h, r

	Layer	Input Size	Bias Term	Leaky Relu α	Output Size
Discriminator D	Linear1+Leaky-Relu	144 or 145	Yes	0.2	72
	Linear2+Leaky-Relu	72	Yes	0.2	36
	Linear3+Softmax	36	Yes	NA	2
Function g_1 & g_2	Linear1+Leaky-Relu	144 or 145	Yes	0.2	144 or 145
	Linear2+Leaky-Relu	144 or 145	Yes	0.2	72
	Linear3+Leaky-Relu	72	Yes	0.2	36
	Linear4+Softmax	36	Yes	NA	5+M
Function h	Linear1+Leaky-Relu	5+M	Yes	0.2	(5+M)*2
	Linear2+Leaky-Relu	(5+M)*2	Yes	0.2	(5+M)*4
	0.2 Dropout+Linear3+Sigmoid	(5+M)*4	Yes	NA	n_{genetic}
Function r	Linear1+Leaky-Relu	$n_{\text{genetic}}+144/145$	Yes	0.2	$(n_{\text{genetic}}+144/145)/2$
	Linear2+Leaky-Relu	$(n_{\text{genetic}}+144/145)/2$	Yes	0.2	$(n_{\text{genetic}}+144/145)/4$
	Linear3+Leaky-Relu	$(n_{\text{genetic}}+144/145)/4$	Yes	0.2	10

eAlgorithm 1: Gene-SGAN training procedure.

l_c represents cross entropy loss and e_i represents a one-hot vector with 1 at the i_{th} component.

while not meeting stopping criteria or reaching max_epoch do

for all batches $\{x^i\}_{i=1}^m, \{y^i\}_{i=1}^m, \{v^i\}_{i=1}^m$ **do**

Perform Phenotype Step with GAN:

Sample m integers $\{a^i\}_{i=1}^m$ with $a^i \sim \text{discrete-U}(1, M)$ and let $z_1^i = e_{a^i}$

Sample m vectors $\{z_2^i\}_{i=1}^m$ from a multivariate uniform distribution with

$z_2^i \sim U[0, 1]^{n_{z_2}}$

Update weights of discriminator D: Use ADAM to update θ_D with gradient:

$$\nabla_{\theta_D} \frac{1}{m} \sum_{i=1}^m [p_{\theta_{z_1}}(z_1^i) (l_c(D(y^i), e_1) + l_c(D(f(x^i, z_1^i, z_2^i), e_0)))]$$

Update weights of functions f, g_1 , and g_2 : Use ADAM to update $\theta_f, \theta_{g_1}, \theta_{g_2}$ with gradient:

$$\nabla_{\theta_f} \frac{1}{m} \sum_{i=1}^m [(p_{\theta_{z_1}}(z_1^i) l_c(D(f(x^i, z_1^i, z_2^i), e_1) + \lambda(l_c(g_1(f(x^i, z_1^i, z_2^i), z_1^i) + \|g_2(f(x^i, z_1^i, z_2^i)) - z_2^i\|_2) + \mu\|f(x^i, z_1^i, z_2^i) - x_i\|_1)]$$

$$\nabla_{\theta_{g_1}} \frac{1}{m} \sum_{i=1}^m [\text{l}_c(g_1(f(x^i, z_1^i, z_2^i), z_1^i))]$$

$$\nabla_{\theta_{g_2}} \frac{1}{m} \sum_{i=1}^m [\|g_2(f(x^i, z_1^i, z_2^i)) - z_2^i\|_2]$$

Update weights of the parametrized distribution $p_{\theta_{z_1}}(z_1)$: Use ADAM to

update θ_{z_1} with gradient:

$$\nabla_{\theta_{z_1}} \frac{1}{m} \sum_{i=1}^m (p_{\theta_{z_1}}(z_1^i) \text{l}_c(D(f(x^i, z_1^i, z_2^i), e_1))) + \kappa D_{\text{KL}}(p_U(z_1) | p_{\theta_{z_1}}(z_1))$$

Perform weight clipping:

$$(\theta_f, \theta_{g_1}, \theta_{g_2}) = \text{clip}((\theta_f, \theta_{g_1}, \theta_{g_2}), -c, c)$$

Perform Gene Step with VI:

Sample m latent vectors $\{z_3^i\}_{i=1}^m$ from m posterior distributions $q_{\theta_r}(z_3^i | v^i, y^i)$ with the reparameterization trick.

Update weights of functions g_1 , h , and r : Use ADAM to update $\theta_r, \theta_h, \theta_{g_1}$ with gradient:

$$\nabla_{\theta_r} \frac{1}{m} \sum_{i=1}^m [\log p_{\theta_h, \theta_{g_1}}(v^i | z_3^i, y^i) + \log p_{z_3}(z_3^i) - \log q_{\theta_r}(z_3^i | v^i, y^i)]$$

$$\nabla_{\theta_h} \frac{1}{m} \sum_{i=1}^m [\log p_{\theta_h, \theta_{g_1}}(v^i | z_3^i, y^i)]$$

$$\nabla_{\theta_{g_1}} \frac{1}{m} \sum_{i=1}^m [\log p_{\theta_h, \theta_{g_1}}(v^i | z_3^i, y^i)]$$

end

end

eMethod 3: Implementation details of model comparisons in the semi-synthetic experiments

For the Gene-SGAN model, we selected the optimal *gene-lr* using the CV procedure (Method 6). Other hyperparameters and network architectures were fixed as introduced in eMethod 2.2. For the other compared methods, the implementation details were introduced in eTable 3. For Smile-GAN, MSC, CCA, and Deep-CCA, we ran models with different combinations of hyperparameters and reported the best performances. For CCA and Deep-CCA, the Kmeans algorithm with $n_init=200$ and $max_iter=500$ was further applied to the outputted embeddings to derive cluster memberships.

eTable 3: Implementation details of the six compared methods.

Model	Package	Features	Hyperparameters
Smile-GAN	SmileGAN 0.1.2	Imaging	$lam = [7,8,9,10,11]$; $mu = [3,4,5,6,7]$;
Kmeans	scikit-learn 0.24.2	Imaging + Genetic	$n_init = 200$; $max_iter=500$;
MKmeans	mvlearn 0.5.0 ⁶	Imaging + Genetic	$n_init = 200$; $max_iter=500$; $patience = 30$;
MSC	mvlearn 0.5.0	Imaging + Genetic	$n_init = 200$; $max_iter = 500$; $affinity = 'nearest\ neighbors'$; $n_neighbors = [30,35,40,45,50]$
CCA	scikit-learn 0.24.2	Imaging + Genetic	$n_components = [3,4,5,6,7,8,9,10]$; $max_iter = 500$
Deep-CCA	mvlearn 0.5.0	Imaging + Genetic	$n_components = [3,4,5,6,7,8,9,10]$; $hidden_layer_size = [128,256,512,1024]$; $n_hidden_layers = 2$; $epoch_num = 1000$;

eMethod 4: Replication analyses for SNP-subtype associations

In the split-sampled experiments on the hypertension dataset, we tested the reproducibility of the SNP-subtype associations found among hypertensive patients in the discovery set. Specifically, we filtered out all significantly associated SNPs after Bonferroni correction in the discovery set. Then, for each SNP, we constructed two M-dimensional vectors, one for the discovery set and one for the replication set. The i_{th} component of the vector equals the MAF of the SNP within the i_{th} subtype. Pearson's correlation between two vectors was calculated for each SNP to analyze consistencies in subtype-wise relationships. Lastly, we used the replication set to retest SNPs with correlations greater than 0.5. We reported the number of significantly associated SNPs after B-H and Bonferroni corrections, respectively.

eMethod 5: Examination of genetic and phenotypic variations captured by z_2 and z_3 .

We examined the latent variables z_2 and z_3 derived by Gene-SGAN on the MCI/AD dataset with $M=4$. After the training process, the inverse mapping function g_2 is applied to patients' imaging ROIs to estimate their z_2 variables. In addition, the function r is applied to concatenated ROIs and AD-associated SNPs to derive the posterior distributions of z_3 . The mean of each derived distribution is used as an estimated z_3 for each participant. We concatenated z_2 across all 50 trained models (**Method 7**) for each participant and derived the first five principal components as z_2 PC1- z_2 PC5. The first five principal components of z_3 , z_3 PC1- z_3 PC5, were derived through the same procedure.

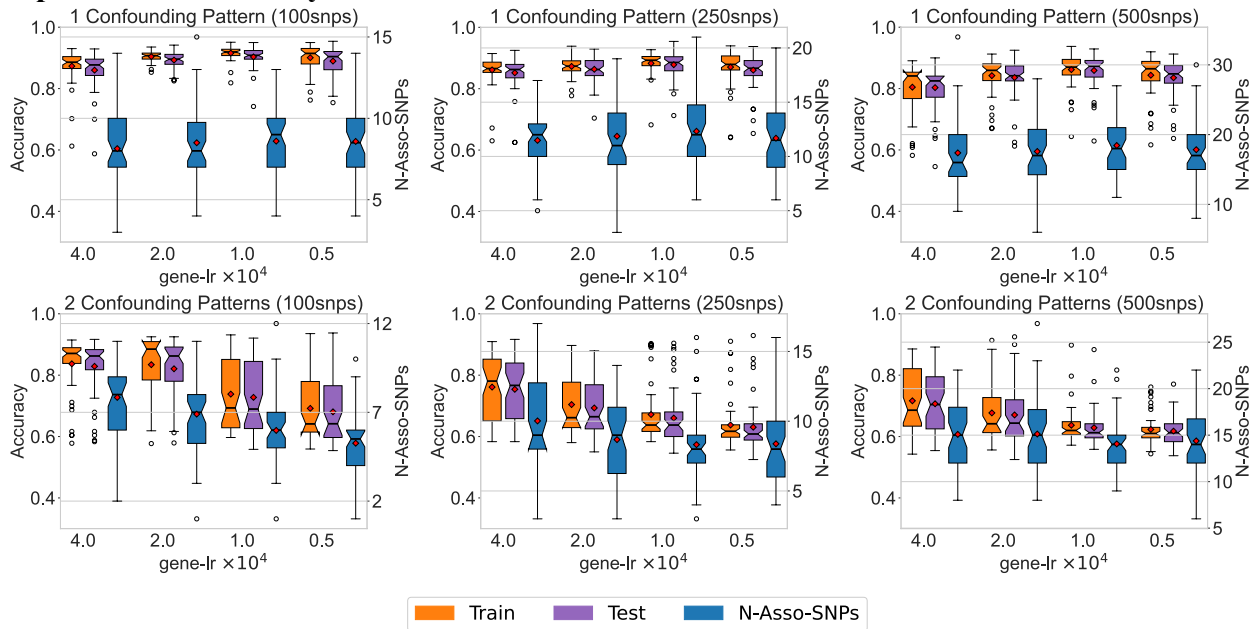
eMethod 5.1 Associations of z_2 and z_3 with imaging volumetric measures.

We performed voxel-based morphometry analyses through Nilearn⁷ and gray matter RAVENS maps⁸. Specifically, we fitted a linear regression model with voxel-wise volumetric measures as dependent variables and each PC as an independent variable, adjusting for covariates including age, gender, ICV, and probabilities of subtypes. Two-tailed t-tests were performed to test associations between each PC and imaging volumetric measures. The Benjamin-Hochberg method was used to correct for multiple comparisons.

eMethod 5.2 Associations of z_2 and z_3 with AD-associated SNPs.

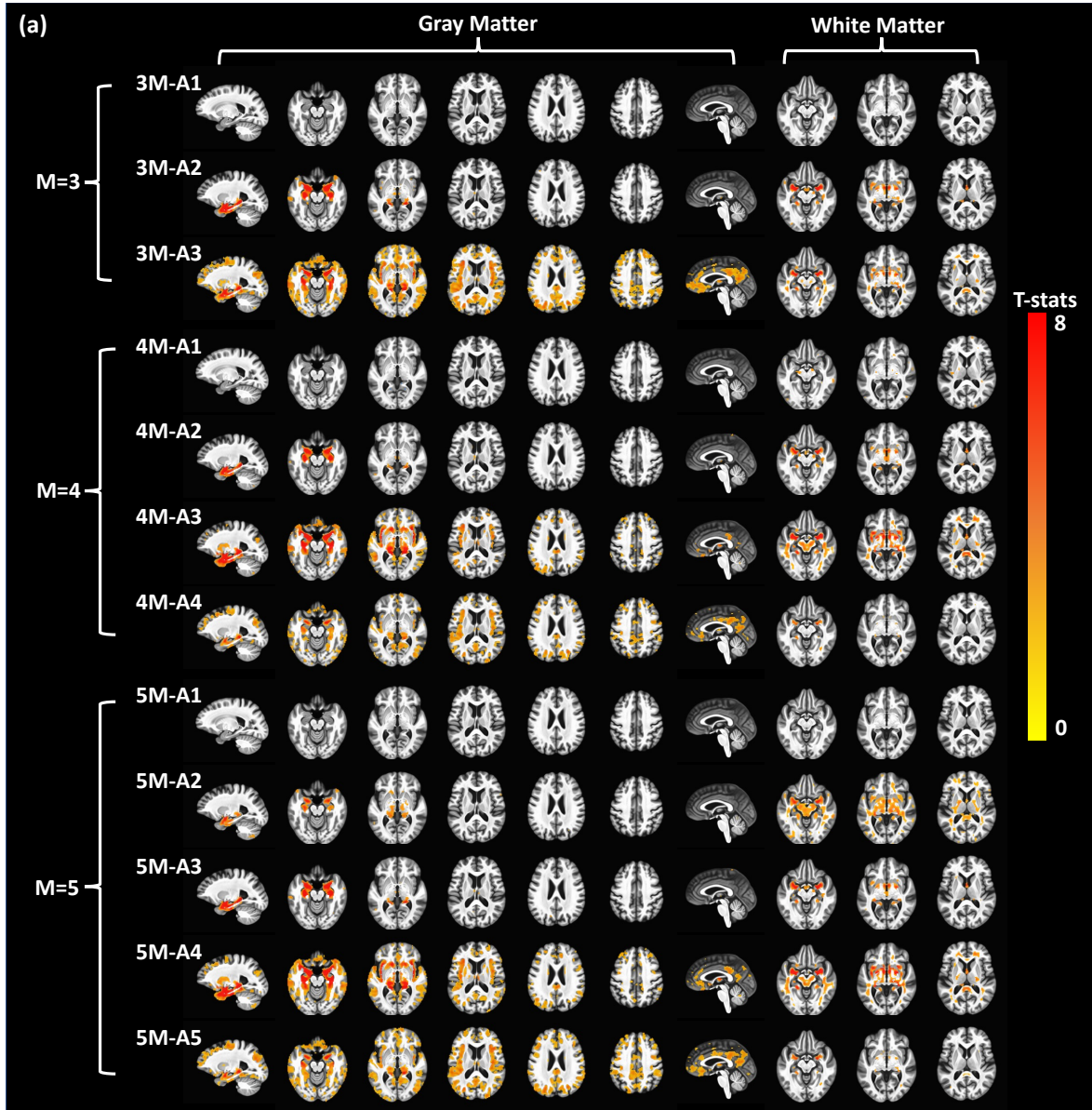
To test associations between each PC of z_2 or z_3 and AD-associated SNPs, we fitted a linear regression model with SNPs as dependent variables and each PC as an independent variable, adjusting for covariates including age, gender, ICV, and probabilities of subtypes. Two-tailed t-tests were performed to test associations between each PC and each SNP, and the Bonferroni method was used to correct for multiple comparisons.

eFigure 1: Gene-SGAN shows robust generalizability to test data in cross validation experiments on semi-synthetic datasets



Gene-SGAN shows robust generalizability to test data. With different hyperparameter (*gene-lr*) settings, SNP data dimensions, and levels of imaging confounder, Gene-SGAN consistently achieves comparable clustering accuracies on the training and test sets. In addition, *N-Asso-SNPs*, the parameter selection metric, was positively correlated with the clustering accuracies, serving as an appropriate metric for suggesting the optimal hyperparameter in real data applications. The left axis reveals the scale of clustering accuracies on the training and test sets (Orange and Purple). The right axis reveals the scale of *N-Asso-SNPs* (blue).

eFigure 2: Gene-SGAN provides consistent and refined multiscale imaging subtypes related to AD.

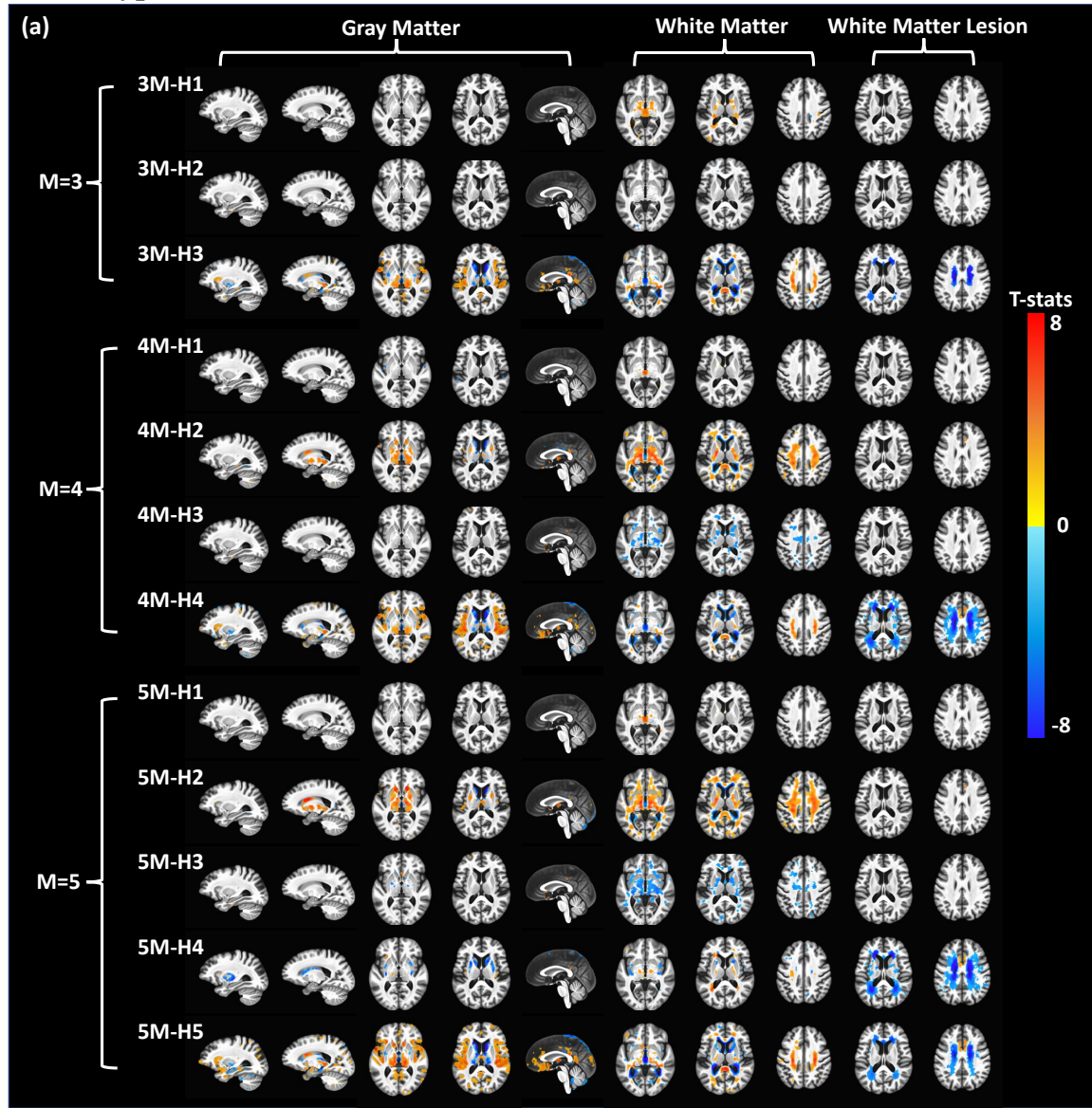


(b)

				4M-A1	4M-A2	4M-A3	4M-A4	
	3M-A1	3M-A2	3M-A3	5M-A1	247 (85.2%)	15 (5.2%)	0	28 (9.6%)
4M-A1	311 (100%)	0	0	5M-A2	59 (50.4%)	36 (30.8%)	20 (17.1%)	2 (1.7%)
4M-A2	22 (11.2%)	169 (85.8%)	6 (3.0%)	5M-A3	2 (1.2%)	144 (83.2%)	15 (8.7%)	12 (6.9%)
4M-A3	2 (0.7%)	108 (38.4%)	171 (60.9%)	5M-A4	0	2 (0.9%)	230 (97.0%)	5 (2.1%)
4M-A4	81 (29.8%)	8 (3.0%)	183 (67.2%)	5M-A5	3 (1.2%)	0	16 (6.6%)	225 (92.2%)

a Voxel-wise group comparisons (two-sided t-test) were performed between the HC group (i.e., cognitively normal participants) and participants dominated by each AD-related subtype derived with different scales $M=3-5$. False discovery rate (FDR) correction for multiple comparisons with a p-value threshold of 0.05 was applied. $xM-Ay$ refers to the y -th AD-related subtype derived by Gene-SGAN with the number of clusters $M=x$. Warmer color denotes more brain atrophy in the subtype versus HC. **b** Tables show the reallocation of participants in refined subtypes. For instance, the data in the first cell of the right table, 247 (85.2%), can be interpreted as 247 participants in 5M-A1 coming from 4M-A1, which is 85.2% of all participants in 5M-A1. The highest fraction in each row is bolded.

eFigure 3: Gene-SGAN provides consistent and refined multiscale imaging subtypes related to hypertension.

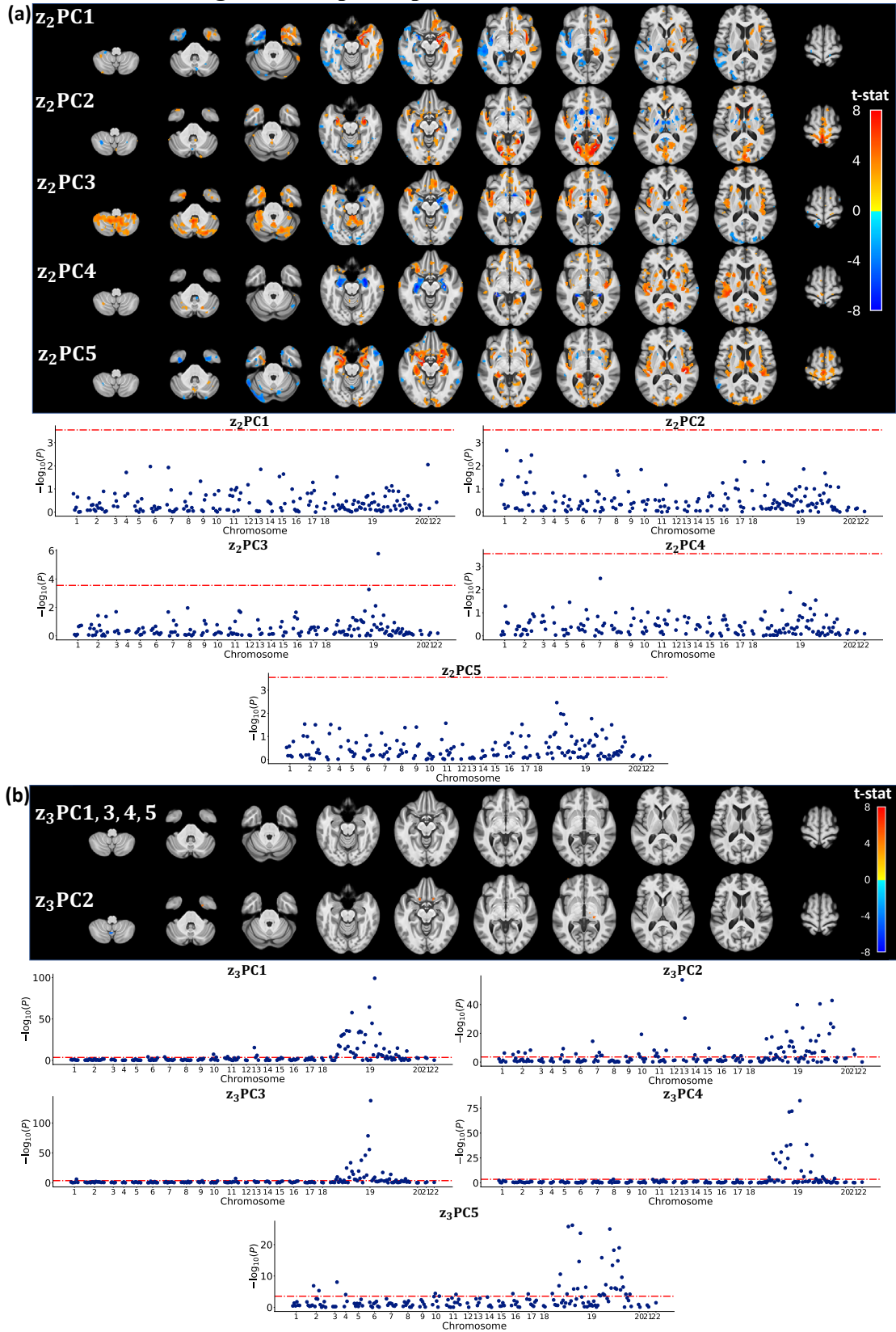


(b)

	3M-H1	3M-H2	3M-H3	5M-H1	4M-H1	4M-H2	4M-H3	4M-H4
3M-H1					4434 (95.3%)	138 (3.0%)	80 (1.7%)	0
4M-H1	4638 (94.1%)	291 (5.9%)	0	5M-H1	274 (7.7%)	3087 (87.1%)	174 (4.9%)	8 (0.2%)
4M-H2	1173 (30.8%)	1938 (50.9%)	699 (18.3%)	5M-H2	216 (4.3%)	29 (0.6%)	4731 (93.8%)	68 (1.3%)
4M-H3	89 (1.6%)	5055 (91.9%)	356 (6.5%)	5M-H3	5 (0.4%)	373 (27.8%)	368 (27.4%)	595 (44.4%)
4M-H4	0 (29.8%)	109 (5.0%)	2066 (95.0%)	5M-H4	0 (1.2%)	183 (10.0%)	147 (8.0%)	1504 (82.0%)

a Voxel-wise statistical comparisons (two-sided t -test) were performed between the HC group (non-hypertensive participants) and participants dominated by each hypertension-related subtype derived with different scales $M=3-5$. FDR correction for multiple comparisons with a p -value threshold of 0.05 was applied. xM -Hy refers to the y -th hypertension-related subtype derived by Gene-SGAN with the number of clusters $M=x$. Warmer color denotes brain atrophy (i.e., HC > subtype), and cooler color represents larger tissue volume (i.e., subtype > HC). **b** Tables show the reallocation of participants in refined subtypes. For instance, data in the first cell of the right table, 4434 (95.3%), can be interpreted as 4434 participants in 5M-H1 coming from 4M-H1, which is 95.3% of all participants in 5M-H1. The highest fraction in each row is bolded.

eFigure 4. z_2 and z_3 variables capture additional non-linked imaging-specific and genetic-specific variations among MCI/AD participants.



a The first five PCs of z_2 primarily capture additional non-genetically associated variations in imaging features, including asymmetry of MTL atrophy (z_2 PC1), atrophy in the cerebellum and cuneus (z_2 PC2 and z_2 PC3), as well as the severity (stages) of brain changes in regions associated with four AD-related subtypes (z_2 PC4 and z_2 PC5). In contrast, only one PC, z_2 PC3, has a significant association with a single SNP. **b** The first five PCs of z_3 mainly capture additional genetic-specific variations without significantly associated imaging patterns. Only z_3 PC2 shows very mild associations with volume changes in the basal forebrain. For voxel-based morphometry analyses, FDR correction was performed to adjust for multiple comparisons with a p-value threshold of 0.05. Warmer color denotes a positive association between voxel-wise volumetric measures and PCs, and cooler color denotes a negative association. In the Manhattan plots, the dashed lines denote the p-value threshold of 0.05 after adjusting for multiple comparisons via the Bonferroni method.

- 1 Goodfellow, I. *et al.* Generative Adversarial Networks. *Advances in Neural Information Processing Systems* **3**, doi:10.1145/3422622 (2014).
- 2 Chen, X. *et al.* InfoGAN: Interpretable Representation Learning by Information Maximizing Generative Adversarial Nets. (2016).
- 3 Yang, Z. *et al.* A deep learning framework identifies dimensional representations of Alzheimer's Disease from brain structure. *Nature Communications* **12**, doi:10.1038/s41467-021-26703-z (2021).
- 4 Kingma, D. & Ba, J. Adam: A Method for Stochastic Optimization. *International Conference on Learning Representations* (2014).
- 5 Arjovsky, M., Chintala, S. & Bottou, L. in *Proceedings of the 34th International Conference on Machine Learning* Vol. 70 (eds Precup Doina & Teh Yee Whye) 214--223 (PMLR, Proceedings of Machine Learning Research, 2017).
- 6 Perry, R. *et al.* *mvlearn: Multiview Machine Learning in Python*. (2020).
- 7 Abraham, A. *et al.* Machine learning for neuroimaging with scikit-learn. *Front Neuroinform* **8**, 14, doi:10.3389/fninf.2014.00014 (2014).
- 8 Davatzikos, C., Genc, A., Xu, D. & Resnick, S. M. Voxel-based morphometry using the RAVENS maps: methods and validation using simulated longitudinal atrophy. *Neuroimage* **14**, 1361-1369, doi:10.1006/nimg.2001.0937 S1053-8119(01)90937-1 [pii] (2001).

Supplementary Data 1. SNPs significantly associated with 3/4/5 AD-related subtypes with and without adjusting for APOE e4

Without APOE e4 adjusted (M=3)

Chr	Position(hg38)	SNP	Closest Genes	Minor Allele	Minor allele frequencies within each subtype			p value
					3M-A1	3M-A2	3M-A3	
19	44908684	rs429358	APOE	C	0.208	0.449	0.39	2.10E-22
19	44898409	rs8106922	TOMM40	G	0.394	0.249	0.297	5.66E-10
19	44909698	rs1081105	APOE/APOC1	C	0.035	0.086	0.083	3.78E-06
19	44926451	rs60049679	APOC1/APOC1P1	C	0.082	0.151	0.146	7.63E-06
19	44878777	rs6859	NECTIN2	A	0.435	0.561	0.524	9.66E-06
19	44928401	rs8106813	APOC1P1	G	0.502	0.382	0.458	3.64E-05
6	32610753	rs9271192	HLA-DRB1/HLA-DQA1	C	0.222	0.304	0.288	9.35E-05
10	11678309	rs7920721	USP6NL-AS1/ECHDC3	G	0.379	0.384	0.468	9.87E-05
19	44839558	rs1466435	BCAM/NECTIN2	C	0.059	0.032	0.022	2.66E-04

With APOE e4 adjusted (M=3)

Chr	Position(hg38)	SNP	Closest Genes	Minor Allele	Minor allele frequencies within each subtype			p value
					3M-A1	3M-A2	3M-A3	
6	136046867	rs11154851	PDE7B	T	0.037	0.063	0.029	5.13E-05
10	11678309	rs7920721	USP6NL-AS1/ECHDC3	G	0.379	0.384	0.468	5.29E-05
6	32610753	rs9271192	HLA-DRB1/HLA-DQA1	C	0.222	0.304	0.288	1.49E-04

Without APOE e4 adjusted (M=4)

Chr	Position(hg38)	SNP	Closest Genes	Minor Allele	Minor allele frequencies within each subtype				p value
					4M-A1	4M-A2	4M-A3	4M-A4	
19	44908684	rs429358	APOE	C	0.199	0.452	0.397	0.34	7.81E-19
19	44898409	rs8106922	TOMM40	G	0.395	0.228	0.274	0.357	2.55E-11
6	32610753	rs9271192	HLA-DRB1/HLA-DQA1	C	0.204	0.299	0.311	0.267	2.91E-06
6	136046867	rs11154851	PDE7B	T	0.039	0.074	0.037	0.026	3.60E-05
19	44926451	rs60049679	APOC1/APOC1P1	C	0.082	0.15	0.157	0.112	3.95E-05
19	44909698	rs1081105	APOE/APOC1	C	0.032	0.079	0.082	0.075	5.03E-05
7	16668236	rs58370486	BZW2	G	0.021	0.038	0.027	0.068	6.62E-05
6	32447376	rs9469112	HLA-DRA/HLA-DRB9	T	0.162	0.234	0.194	0.147	9.96E-05
10	11678309	rs7920721	USP6NL-AS1/ECHDC3	G	0.37	0.373	0.427	0.467	1.49E-04
19	44879835	rs71171301	NECTIN2	AC	0.109	0.155	0.171	0.14	2.44E-04

With APOE e4 adjusted (M=4)

Chr	Position(hg38)	SNP	Closest Genes	Minor Allele	Minor allele frequencies within each subtype				p value
					4M-A1	4M-A2	4M-A3	4M-A4	
6	136046867	rs11154851	PDE7B	T	0.039	0.074	0.037	0.026	3.23E-06
6	32610753	rs9271192	HLA-DRB1/HLA-DQA1	C	0.204	0.299	0.311	0.267	4.15E-06
10	11678309	rs7920721	USP6NL-AS1/ECHDC3	G	0.37	0.373	0.427	0.467	1.15E-04
7	16668236	rs58370486	BZW2	G	0.021	0.038	0.027	0.068	1.45E-04
10	17846684	rs4748424	MRC1	G	0.161	0.104	0.117	0.105	2.39E-04
6	32447376	rs9469112	HLA-DRA/HLA-DRB9	T	0.162	0.234	0.194	0.147	2.75E-04

Without APOE e4 adjusted (M=5)

Chr	Position(hg38)	SNP	Closest Genes	Minor Allele	Minor allele frequencies within each subtype					p value
					5M-A1	5M-A2	5M-A3	5M-A4	5M-A5	
19	44908684	rs429358	APOE	C	0.217	0.222	0.497	0.424	0.326	1.46E-23
19	44898409	rs8106922	TOMM40	G	0.383	0.385	0.22	0.249	0.365	7.65E-13
19	44926451	rs60049679	APOC1/APOC1P1	C	0.086	0.068	0.171	0.169	0.111	8.34E-08
6	32610753	rs9271192	HLA-DRB1/HLA-DQA1	C	0.221	0.197	0.309	0.331	0.26	9.48E-08
19	44909698	rs1081105	APOE/APOC1	C	0.04	0.021	0.084	0.095	0.074	4.98E-07
19	44879835	rs71171301	NECTIN2	AC	0.1	0.158	0.182	0.173	0.125	9.79E-07
11	14202800	rs11023139	SPON1	A	0.052	0.09	0.075	0.019	0.043	3.28E-06
19	44928401	rs8106813	APOC1P1	G	0.521	0.419	0.39	0.407	0.488	1.15E-05
19	45012792	rs35194383	RELB	T	0.434	0.406	0.535	0.485	0.465	2.34E-05
19	44878777	rs6859	NECTIN2	A	0.436	0.47	0.572	0.54	0.496	4.59E-05
6	32615580	rs6931277	HLA-DRB1/HLA-DQA1	T	0.179	0.158	0.145	0.122	0.201	1.42E-04
7	16668236	rs58370486	BZW2	G	0.028	0.034	0.035	0.023	0.068	2.45E-04
19	44905371	rs769446	TOMM40/APOE	C	0.084	0.064	0.055	0.105	0.057	2.69E-04

With APOE e4 adjusted (M=5)

Chr	Position(hg38)	SNP	Closest Genes	Minor Allele	Minor allele frequencies within each subtype					p value
					5M-A1	5M-A2	5M-A3	5M-A4	5M-A5	
6	32610753	rs9271192	HLA-DRB1/HLA-DQA1	C	0.221	0.197	0.309	0.331	0.260	1.77E-07
11	14202800	rs11023139	SPON1	A	0.052	0.090	0.075	0.019	0.043	4.57E-06
6	32615580	rs6931277	HLA-DRB1/HLA-DQA1	T	0.179	0.158	0.145	0.122	0.201	1.26E-04
19	44879835	rs71171301	NECTIN2	AC	0.100	0.158	0.182	0.173	0.125	1.44E-04
6	136046867	rs11154851	PDE7B	T	0.040	0.060	0.064	0.030	0.031	2.02E-04
19	44794671	rs2889414	CBLC	G	0.424	0.329	0.364	0.376	0.426	2.03E-04
19	44892009	rs157580	TOMM40	G	0.328	0.368	0.263	0.310	0.268	2.12E-04

Supplementary Data 2. plasma/CSF biomarkers that are significantly different among four AD-related subtypes

name	4M-A1	4M-A2	4M-A3	4M-A4	p value
Angiotensin-Converting Enzyme (ACE) (ng/ml)	0.407+-0.164	0.333+-0.157	0.261+-0.139	0.257+-0.156	3.84E-05
Chromogranin-A (CgA) (ng/ml)	290.882+-54.855	297.372+-44.761	252.07+-53.002	267.026+-50.383	6.09E-05
von Willebrand Factor (vWF) (ug/ml)	-1.369+-0.134	-1.442+-0.161	-1.454+-0.139	-1.537+-0.163	8.46E-05
Heparin-Binding EGF-Like Growth Factor ((pg/ml)	2.474+-0.098	2.454+-0.11	2.385+-0.093	2.415+-0.105	2.29E-04
Tissue Factor (TF) (ng/ml)	0.644+-0.218	0.643+-0.214	0.489+-0.173	0.553+-0.183	2.30E-04
Cortisol (ng/mL)	2.131+-0.11	2.186+-0.12	2.206+-0.143	2.156+-0.141	2.98E-04
Monokine Induced by Gamma Interferon (MI (pg/ml)	2.465+-0.368	2.343+-0.31	2.474+-0.326	2.2+-0.318	5.05E-04
Cystatin-C (ng/ml)	0.4+-0.094	0.399+-0.092	0.461+-0.074	0.441+-0.081	6.02E-04
Macrophage Colony-Stimulating Factor 1 ((ng/mL)	-0.161+-0.137	-0.226+-0.144	-0.278+-0.121	-0.27+-0.145	6.58E-04
CD 40 antigen (CD40) (ng/mL)	-0.587+-0.118	-0.609+-0.129	-0.666+-0.101	-0.679+-0.12	1.00E-03
Vascular Endothelial Growth Factor (VEGF (pg/mL)	2.815+-0.123	2.768+-0.103	2.827+-0.135	2.781+-0.106	1.05E-03
Tamm-Horsfall Urinary Glycoprotein (THP) (ug/mL)	-1.431+-0.199	-1.323+-0.165	-1.397+-0.181	-1.37+-0.184	1.05E-03
Vascular Endothelial Growth Factor (VEGF (pg/mL)	2.761+-0.135	2.738+-0.146	2.661+-0.107	2.687+-0.129	1.39E-03
B Lymphocyte Chemoattractant (BLC) (pg/mL)	1.441+-0.157	1.385+-0.205	1.498+-0.222	1.447+-0.221	1.76E-03
AXL Receptor Tyrosine Kinase (AXL) (ng/mL)	4.685+-1.626	4.579+-1.725	3.689+-1.204	3.911+-1.216	2.30E-03
Transforming Growth Factor alpha (TGF- α) (pg/mL)	1.043+-0.308	1.106+-0.213	0.908+-0.326	1.06+-0.213	2.96E-03
Trefoil Factor 3 (TFF3) (ug/ml)	-1.677+-0.204	-1.736+-0.184	-1.777+-0.168	-1.836+-0.196	3.54E-03
CD 40 antigen (CD40) (ng/mL)	-0.133+-0.172	-0.152+-0.128	-0.087+-0.121	-0.134+-0.119	3.63E-03

Blue: CSF biomarkers

Green: Plasma biomarkers

Supplementary Data 3. SNPs significantly associated with 3/4/5 hypertension-related subtypes

M=3

Chr	Position(hg38)	SNP	Closest Genes	Minor Allele	Minor allele frequencies within each subtype			p value
					3M-H1	3M-H2	3M-H3	
16	87199579	rs4843553	<i>C16orf95</i>	A	0.428	0.424	0.379	5.27E-12
2	203144334	rs72934583	<i>NBEAL1</i>	G	0.136	0.128	0.106	1.43E-09
6	31463022	rs2596473	<i>LINC01149/HCP5</i>	T	0.457	0.481	0.485	1.42E-05
2	55923729	rs3762515	<i>EFEMP1</i>	T	0.089	0.096	0.109	1.67E-05
16	51408768	rs1948948	<i>LOC102723323</i>	T	0.445	0.450	0.420	3.66E-05
6	150697773	rs6940540	<i>PLEKHG1</i>	G	0.401	0.403	0.431	8.50E-05
10	103146454	rs11191580	<i>NT5C2</i>	C	0.069	0.074	0.085	1.16E-04
11	47419207	rs2293579	<i>PSMC3</i>	A	0.391	0.402	0.371	1.55E-04

M=4

Chr	Position(hg38)	SNP	Closest Genes	Minor Allele	Minor allele frequencies within each subtype				p value
					4M-H1	4M-H2	4M-H3	4M-H4	
16	87199579	rs4843553	<i>C16orf95</i>	A	0.433	0.409	0.431	0.369	1.20E-16
10	103146454	rs11191580	<i>NT5C2</i>	C	0.065	0.071	0.079	0.087	5.71E-08
2	203144334	rs72934583	<i>NBEAL1</i>	G	0.137	0.129	0.124	0.110	3.86E-07
11	47419207	rs2293579	<i>PSMC3</i>	A	0.406	0.374	0.401	0.377	6.09E-07
6	31463022	rs2596473	<i>LINC01149/HCP5</i>	T	0.460	0.461	0.486	0.489	2.00E-06
6	150697773	rs6940540	<i>PLEKHG1</i>	G	0.403	0.403	0.401	0.435	2.61E-05
11	47879717	rs1872167	<i>NUP160</i>	T	0.136	0.148	0.127	0.141	3.17E-05
16	51408768	rs1948948	<i>LOC102723323</i>	T	0.441	0.450	0.450	0.418	3.50E-05
10	103850568	rs10786772	<i>SH3PXD2A</i>	A	0.373	0.362	0.367	0.341	5.13E-05
2	42893609	rs11685652	<i>CHORDC1P1</i>	A	0.207	0.191	0.194	0.182	6.48E-05
2	55923729	rs3762515	<i>EFEMP1</i>	T	0.088	0.099	0.095	0.107	7.32E-05
6	20679478	rs7756992	<i>CDKAL1</i>	G	0.256	0.250	0.272	0.268	1.47E-04
6	33073957	rs2856830	<i>HLA-DPA1</i>	C	0.123	0.109	0.110	0.107	2.03E-04

M=5

Chr	Position(hg38)	SNP	Closest Genes	Minor Allele	Minor allele frequencies within each subtype					p value
					5M-H1	5M-H2	5M-H3	5M-H4	5M-H5	
2	203144334	rs72934583	<i>NBEAL1</i>	G	0.139	0.129	0.130	0.090	0.112	2.22E-15
16	87199579	rs4843553	<i>C16orf95</i>	A	0.429	0.406	0.433	0.406	0.377	7.46E-12
10	103146454	rs11191580	<i>NT5C2</i>	C	0.063	0.071	0.079	0.077	0.091	2.17E-09
11	47419207	rs2293579	<i>PSMC3</i>	A	0.403	0.376	0.406	0.373	0.374	9.24E-08
11	47879717	rs1872167	<i>NUP160</i>	T	0.135	0.147	0.125	0.153	0.143	8.19E-07
6	31463022	rs2596473	<i>LINC01149/HCP5</i>	T	0.457	0.465	0.482	0.495	0.489	1.88E-06
2	55923729	rs3762515	<i>EFEMP1</i>	T	0.086	0.097	0.096	0.112	0.104	6.29E-06
3	183662247	rs830179	<i>KLHL24</i>	A	0.332	0.313	0.317	0.313	0.296	1.25E-05
6	20679478	rs7756992	<i>CDKAL1</i>	G	0.255	0.251	0.275	0.248	0.270	1.60E-05
4	102267552	rs13107325	<i>SLC39A8</i>	T	0.064	0.064	0.077	0.064	0.064	1.67E-05
10	103850568	rs4630220	<i>SH3PXD2A</i>	A	0.291	0.270	0.289	0.264	0.268	2.54E-05
17	2056532	rs112963849	<i>HIC1</i>	A	0.087	0.076	0.092	0.076	0.083	2.60E-05
8	11173963	rs7004825	<i>XKR6</i>	T	0.484	0.464	0.466	0.493	0.455	2.76E-05
22	50289633	rs28379706	<i>PLXNB2</i>	C	0.388	0.379	0.400	0.384	0.414	3.12E-05
5	122182683	rs2303655	<i>ZNF474-AS1</i>	C	0.192	0.197	0.184	0.165	0.177	3.77E-05
10	103850568	rs10786772	<i>SH3PXD2A</i>	A	0.370	0.368	0.368	0.339	0.345	4.14E-05
14	91415043	rs1285841	<i>CCDC88C</i>	T	0.444	0.446	0.435	0.408	0.452	7.72E-05
1	43420823	rs2782643	<i>SZT2</i>	T	0.422	0.429	0.402	0.409	0.418	8.01E-05
17	75894282	rs55823223	<i>TRIM65</i>	A	0.143	0.137	0.142	0.166	0.154	8.94E-05
6	150697773	rs6940540	<i>PLEKHG1</i>	G	0.401	0.404	0.402	0.434	0.425	9.43E-05
15	74776941	rs936226	<i>CYP1A2/CSK</i>	C	0.275	0.274	0.266	0.275	0.244	1.21E-04
14	22940700	rs35085068	<i>PRMT5/HAUS4</i>	C	0.428	0.443	0.428	0.418	0.404	1.28E-04
6	33073957	rs2856830	<i>HLA-DPA1</i>	C	0.123	0.111	0.109	0.111	0.105	1.64E-04
7	134510938	rs782513	<i>AKR1B1/AKR1B10</i>	C	0.433	0.435	0.428	0.404	0.410	1.86E-04
8	54345567	rs10103692	<i>RNU105C/RN7SL2</i>	G	0.086	0.092	0.088	0.109	0.089	2.97E-04
16	51408768	rs1948948	<i>LOC102723323</i>	T	0.443	0.447	0.450	0.436	0.418	3.32E-04
10	61764833	rs1530440	<i>CABCOCO1</i>	T	0.193	0.178	0.183	0.169	0.178	3.84E-04

Supplementary Data 4. Replication Analyses on hypertension-related subtypes: SNPs significantly associated with 5 hypertension-related subtypes on discovery set

Chr	Position(hg38)	SNP	Closest Genes	Minor Allele	Discovery Set						Replication Set						
					Minor allele frequencies within each subtype						Minor allele frequencies within each subtype						
					5M-H1	5M-H2	5M-H3	5M-H4	5M-H5	p_value	5M-H1	5M-H2	5M-H3	5M-H4	5M-H5	Correlation	p value
2	203144334	rs72934583	<i>NBEAL1</i>	G	0.097	0.086	0.124	0.125	0.150	3.92E-15	0.116	0.129	0.134	0.139	0.132	0.544	2.54E-03
16	87199579	rs4843553	<i>C16orf95</i>	A	0.386	0.432	0.441	0.403	0.430	7.05E-08	0.384	0.415	0.421	0.411	0.432	0.852	8.98E-05
10	103146454	rs11191580	<i>NT5C2</i>	C	0.087	0.077	0.079	0.070	0.061	5.25E-06	0.084	0.070	0.082	0.068	0.065	0.899	6.45E-04
11	10247046	rs56352102	<i>SBF2</i>	T	0.185	0.151	0.200	0.184	0.204	7.07E-06	0.173	0.172	0.185	0.187	0.195	0.764	1.33E-02
14	22940700	rs35085068	<i>PRMT5/HAUS4</i>	C	0.392	0.457	0.423	0.433	0.440	1.40E-05	0.415	0.447	0.429	0.446	0.420	0.692	3.85E-03
22	50289633	rs28379706	<i>PLXNB2</i>	C	0.407	0.401	0.414	0.373	0.384	2.03E-05	0.393	0.389	0.388	0.389	0.377	0.404	1.39E-01
12	111472415	rs10774625	<i>ATXN2</i>	A	0.513	0.515	0.491	0.513	0.479	8.70E-05	0.500	0.492	0.496	0.494	0.502	-0.630	4.49E-01
17	75894282	rs55823223	<i>TRIM65</i>	A	0.164	0.127	0.141	0.137	0.132	1.26E-04	0.150	0.163	0.152	0.140	0.150	-0.289	5.18E-02
11	47419207	rs2293579	<i>PSMC3</i>	A	0.379	0.388	0.400	0.371	0.408	1.29E-04	0.367	0.368	0.412	0.385	0.408	0.725	4.35E-05
6	150697773	rs6940540	<i>PLEKHG1</i>	G	0.439	0.414	0.397	0.401	0.410	1.93E-04	0.417	0.423	0.405	0.399	0.392	0.545	3.10E-02
2	55923729	rs3762515	<i>EFEMP1</i>	T	0.105	0.114	0.095	0.098	0.084	2.39E-04	0.111	0.098	0.097	0.095	0.085	0.691	7.79E-04
6	31720741	rs805293	<i>LY6G6C/MPIG6B</i>	A	0.454	0.477	0.471	0.457	0.437	2.98E-04	0.469	0.469	0.447	0.447	0.432	0.593	3.17E-03
3	183662247	rs830179	<i>KLHL24</i>	A	0.303	0.309	0.321	0.313	0.341	2.98E-04	0.320	0.337	0.300	0.319	0.312	-0.489	1.53E-02
5	122182683	rs2303655	<i>ZNF474-AS1</i>	C	0.171	0.171	0.180	0.199	0.194	3.59E-04	0.177	0.180	0.189	0.189	0.197	0.814	6.93E-02
7	27181212	rs6461992	<i>HOXA11</i>	A	0.072	0.049	0.069	0.074	0.078	3.61E-04	0.068	0.053	0.076	0.075	0.073	0.904	5.13E-03

Supplementary Data 5a. Replication Analyses on hypertension-related subtypes derived by Smile-GAN: SNPs significantly associated with subtypes on discovery set

Chr	Position(hg38)	SNP	Closest Genes	Minor Allele	Discovery Set						Replication Set						
					Minor allele frequencies within each subtype						Minor allele frequencies within each subtype						
					5M-H1	5M-H2	5M-H3	5M-H4	5M-H5	p value	5M-H1	5M-H2	5M-H3	5M-H4	5M-H5	Correlation	p value
2	203144334	rs72934583	NBEAL1	G	0.130	0.124	0.140	0.102	0.112	5.98E-07	0.141	0.135	0.127	0.126	0.129	0.351	2.81E-02
16	87199579	rs4843553	C16orf95	A	0.424	0.412	0.440	0.387	0.434	1.60E-05	0.433	0.414	0.409	0.385	0.429	0.718	6.52E-05
3	183662247	rs830179	KLHL24	A	0.335	0.295	0.335	0.306	0.312	1.12E-04	0.316	0.324	0.322	0.305	0.300	0.170	1.50E-02
17	75894282	rs55823223	TRIM65	A	0.132	0.143	0.128	0.152	0.155	2.72E-04	0.152	0.135	0.148	0.151	0.157	0.236	2.69E-02
5	32830415	rs1173727	NPR3/SH3PXD2B	T	0.384	0.389	0.388	0.388	0.424	2.96E-04	0.391	0.397	0.394	0.390	0.379	-0.903	1.41E-01

Supplementary Data 5b. SNPs significantly associated with hypertension-related subtypes derived by Smile-GAN on discovery+replication sets

Chr	Position(hg38)	SNP	Closest Genes	Minor Allele	Minor allele frequencies within each subtype					
					5M-H1	5M-H2	5M-H3	5M-H4	5M-H5	p value
16	87199579	rs4843553	C16orf95	A	0.416	0.387	0.419	0.435	0.428	2.88E-09
2	55923729	rs3762515	EFEMP1	T	0.089	0.108	0.096	0.091	0.100	1.91E-05
10	103146454	rs11191580	NT5C2	C	0.068	0.079	0.083	0.071	0.069	2.70E-05
8	11173963	rs7004825	XKR6	T	0.467	0.463	0.471	0.471	0.502	1.22E-04
2	203144334	rs72934583	NBEAL1	G	0.134	0.118	0.121	0.131	0.130	2.50E-04
15	74776941	rs936226	CYP1A2/CSK	C	0.279	0.262	0.255	0.275	0.273	2.73E-04
6	20679478	rs7756992	CDKAL1	G	0.249	0.262	0.269	0.270	0.251	2.76E-04
6	31463022	rs2596473	LINC01149/HCP5	T	0.461	0.481	0.487	0.469	0.465	2.91E-04

Supplementary Data 6. ROIs included in the simulated imaging patterns for the semi-synthetic experiments.

ROI index	ROI name
0	Right Amygdala
1	Left Amygdala
2	Right Hippocampus
3	Left Hippocampus
4	Left Basal Forebrain
5	Right Basal Forebrain
6	Right Ent entorhinal area
7	Left Ent entorhinal area
8	Right ITG inferior temporal gyrus
9	Left ITG inferior temporal gyrus
10	Right PHG parahippocampal gyrus
11	Left PHG parahippocampal gyrus
12	RightTMP temporal pole
13	Left TMP temporal pole
14	Right FO frontal operculum
15	Left FO frontal operculum
16	Right MFC medial frontal cortex
17	Left MFC medial frontal cortex
18	Right MFG middle frontal gyrus
19	Left MFG middle frontal gyrus
20	Right OpIFG opercular part of the inferior frontal gyrus
21	Left OpIFG opercular part of the inferior frontal gyrus
22	Right Plns posterior insula
23	Left Plns posterior insula
24	Right TrIFG triangular part of the inferior frontal gyrus
25	Left TrIFG triangular part of the inferior frontal gyrus
26	Right SOG superior occipital gyrus
27	Left SOG superior occipital gyrus
28	Right Calc calcarine cortex
29	Left Calc calcarine cortex
30	Right Cun cuneus
31	Left Cun cuneus
32	Left MOG middle occipital gyrus
33	Right MOrG medial orbital gyrus
34	Right IOG inferior occipital gyrus
35	Left IOG inferior occipital gyrus
36	Right LiG lingual gyrus
37	Left LiG lingual gyrus
38	Right Caudate
39	Left Caudate
40	Right Pallidum
41	Left Pallidum
42	Right Putamen
43	Left Putamen
44	Right Thalamus Proper
45	Left Thalamus Proper
46	fornix right
47	fornix left
48	anterior limb of internal capsule right
49	anterior limb of internal capsule left